



# The Eddington ratio-dependent ‘changing look’ events in NGC 2992

Muryel Guolo <sup>1,2\*</sup>, Daniel Ruschel-Dutra,<sup>1</sup> Dirk Grupe <sup>3</sup>, Bradley M. Peterson,<sup>4,5</sup>  
Thaisa Storchi-Bergmann,<sup>6</sup> Jaderson Schimoia,<sup>7</sup> Rodrigo Nemmen<sup>8</sup> and Andrew Robinson<sup>9</sup>

<sup>1</sup>*Departamento de Física - CFM - Universidade Federal de Santa Catarina, 476, Florianópolis SC 88040-900, Brazil*

<sup>2</sup>*Department of Physics and Astronomy, Johns Hopkins University, 3400 N. Charles St., Baltimore MD 21218, USA*

<sup>3</sup>*Space Science Center, Morehead State University, 235 Martindale Drive, Morehead KY 40351, USA*

<sup>4</sup>*Department of Astronomy, The Ohio State University, 140 W 18th Ave, Columbus OH 43210, USA*

<sup>5</sup>*Center for Cosmology and AstroParticle Physics, 191 Woodruff Ave., Columbus OH 43210, USA*

<sup>6</sup>*Departamento de Astronomia, Universidade Federal do Rio Grande do Sul. Av. Bento Gonçalves 9500, Porto Alegre RS 91501-970, Brazil*

<sup>7</sup>*Departamento de Física - CCNE - Universidade Federal de Santa Maria, 97105-90 Santa Maria, RS, Brazil*

<sup>8</sup>*Instituto de Astronomia, Geofísica e Ciências Atmosféricas, Universidade de São Paulo, São Paulo SP 05508-090, Brazil*

<sup>9</sup>*School of Physics and Astronomy, Rochester Institute of Technology, 84 Lomb Memorial Drive, Rochester NY 14623, USA*

Accepted 2021 September 6. Received 2021 August 24; in original form 2020 November 3

## ABSTRACT

We present an analysis of historical multiwavelength emission of the ‘Changing Look’ (CL) Active Galactic Nucleus (AGN) in NGC 2992, covering epochs ranging from 1978 to 2021, as well as new X-ray and optical spectra. The galaxy presents multiple Seyfert type transitions from Type 2 to intermediate-type, losing and regaining its H $\alpha$  broad emission lines (BEL) recurrently. In X-rays, the source shows intrinsic variability with the absorption corrected luminosity varying by a factor of  $\sim 40$ . We rule-out tidal disruption events or variable obscuration as causes of the type transitions, and show that the presence and the flux of the H $\alpha$  BEL is directly correlated with the 2–10 keV X-ray luminosity ( $L_{2-10}$ ): the component disappears at  $L_{2-10} \leq 2.6 \times 10^{42} \text{ erg cm}^{-2} \text{ s}^{-1}$ ; this luminosity value translates into an Eddington ratio ( $\lambda_{\text{Edd}}$ ) of  $\sim 1$  per cent. The  $\lambda_{\text{Edd}}$  in which the BEL transitions occur is the same as the critical value at which a state transition between a radiatively inefficient accretion flow and a thin accretion disk is expected, such similarity suggests that the AGN is operating at the threshold mass accretion rate between the two accretion modes. We find a correlation between the narrow Fe K $\alpha$  flux and  $\lambda_{\text{Edd}}$ , and an anticorrelation between full-width at half maximum of H $\alpha$  BEL and  $\lambda_{\text{Edd}}$ , in agreement with theoretical predictions. Two possible scenarios for type transitions are compatible with our results: either the dimming of the AGN continuum, which reduces the supply of ionizing photons available to excite the gas in the Broad Line Region (BLR), or the fading of the BLR structure itself occurs as the low accretion rate is not able to sustain the required cloud flow rate in a disc-wind BLR model.

**Key words:** galaxies: nuclei – galaxies: Seyfert – X-rays: galaxies.

## 1 INTRODUCTION

Supermassive black holes (SMBH) at the centre of galaxies can become active by the accretion of surrounding matter (see Storchi-Bergmann & Schnorr-Müller 2019, for a review on the feeding mechanisms). Such active galactic nuclei (AGN) can be identified by features in their optical spectra – such as broad emission lines (BEL) and/or narrow high-ionization emission lines due to the non-stellar ionizing continuum – or by their nuclear X-ray emission. Emission lines produced by the gas present in the vicinity of the SMBH are Doppler broadened, forming the broad-line region (BLR), while the narrow-line region (NLR) extends from a few parsecs to hundreds of parsecs beyond the accretion disc. Historically, Type 1 AGNs are those showing both broad ( $>10^3$ ,  $<10^4 \text{ km s}^{-1}$ ) and narrow ( $<10^3 \text{ km s}^{-1}$ ) permitted emission lines and narrow forbidden lines in their optical spectra; while Type 2 AGNs lack BELs. Intermediate AGN types were added by Osterbrock (1981), including types 1.8 and

1.9, classified, respectively, according to the presence of a weak, or absent, H $\beta$  BEL, while retaining an H $\alpha$  BEL.

AGN unification models attribute differences in AGN type to the viewing angle toward an axisymmetric, parsec scale obscuring structure, which can block our direct view of the AGN central engine (Antonucci 1993; Urry & Padovani 1995) and is responsible for the lack of BEL in Type 2 AGNs. However, a relatively small number of AGN show transitions from one type to another in a few years; these objects are known as ‘changing look’ (CL) AGNs. CL-AGNs have changed the widely accepted AGN paradigm, not only in the orientation-based unified model but also standard accretion disc models (see Lawrence 2018, for a review of the so-called Quasar viscosity crisis). Their extreme and fast variability has motivated alternatives and/or modifications for both the AGN unified model (e.g. Nicastro 2000; Elitzur & Shlosman 2006; Elitzur, Ho & Trump 2014) and for the standard Shakura & Sunyaev (1973) accretion disc model (e.g. Jiang & Blaes 2020; Sniegowska et al. 2020).

Until recently there were only a handful of CL events reported, including NGC 3516 (Andrillat & Souffrin 1971), NGC 1566

\* E-mail: [mguolop1@jhu.edu](mailto:mguolop1@jhu.edu)

(Pastoriza & Gerola 1970; Oknyansky et al. 2019), Mrk 590 (Denney et al. 2014), NGC 2617 (Shappee et al. 2014), NGC 7603 (Tohline & Osterbrock 1976), Mrk 1018 (Cohen et al. 1986), NGC 1097 (Storchi-Bergmann, Baldwin & Wilson 1993), NGC 3065 (Eracleous & Halpern 2001), and NGC 7582 (Aretxaga et al. 1999). In 2015 LaMassa et al. discovered the first CL Quasar and since then the number of known CL-AGNs has increased rapidly (e.g. MacLeod et al. 2016; McElroy et al. 2016; Ruan et al. 2016; Runnoe et al. 2016; Sheng et al. 2017; Kollatschny et al. 2018; Yang et al. 2018; Graham et al. 2019, 2020; Guo et al. 2019; Wang et al. 2019; Kollatschny et al. 2020); however, the number is still fewer than a hundred. Although rare, these objects provide valuable constraints for our models of the central engine.

Some of these CL might be successfully explained via variable obscuration (e.g. Matt, Guainazzi & Maiolino 2003; Puccetti et al. 2007; Risaliti et al. 2010; Marchese et al. 2012; Marinucci et al. 2013): in models where the obscuring material has a patchy distribution (e.g. Nenkova et al. 2008; Elitzur 2012), the dynamical movement of the dust clouds could result in a change of classification. Transient events such as tidal disruption events (TDE) of a star by the SMBH were also claimed as possible drivers of CL events (Eracleous et al. 1995); however, this scenario does not apply to sources presenting multiple (and quasi-periodic) CL events.

In a third scenario, it has been argued that changes in type are expected with variations in accretion rate. In this scenario either the BELs disappear (reappear) due to the reduction (increase) of ionizing photons available to excite the gas in the vicinity of the black hole (e.g. Storchi-Bergmann et al. 2003; LaMassa et al. 2015) or the BLR itself disappears, given that in disc-wind BLR models (e.g. Nicastro 2000; Elitzur & Shlosman 2006; Elitzur & Ho 2009) the broad line emission region follows an evolutionary sequence that is directly related to the accretion rate of the compact source. In such disc-wind BLR models, a low accretion efficiency is not able to sustain the required cloud flow rate responsible for the formation of the BLR clouds, which gives origin to the distinct (intrinsic) AGN types, as proposed by Elitzur et al. (2014).

NGC 2992 is a highly inclined,  $i \sim 70^\circ$ , nearby ( $z = 0.00771$ ; Keel 1996) Seyfert galaxy. The galaxy was the subject of several studies and target of all major X-ray missions due to its variability. In the X-rays, it steadily declined in observed flux from 1978, when it was observed by *HEAOI* (Mushotzky 1982) at a flux level of about  $8 \times 10^{-11} \text{ erg cm}^{-2} \text{ s}^{-1}$  until 1994 when it was observed by *ASCA* (Weaver et al. 1996) at a fainter flux level by about a factor of 20. Then it underwent a rapid recovery: in 1997 it was observed by *BeppoSAX* at a flux level somewhat higher than in 1994, while in 1998 the source fully recovered its *HEAOI* brightness (Gilli et al. 2000). In 2003, when observed by *XMM-Newton*, the flux was even higher, about  $10^{-10} \text{ erg cm}^{-2} \text{ s}^{-1}$  (Shu et al. 2010). The source was then observed by *SUZAKU* on 2005 November or December, and found in a much fainter state, almost an order of magnitude fainter than in the *XMM-Newton* observation.

The *Ross X-ray Timing Explorer (RXTE)*; Swank 2006) monitoring campaign between 2005 early March and 2006 late January found large amplitude (almost an order of magnitude) variability, indicating that apart from the long-term variability of the source, it also presents short-term outbursts with variations in the order of days, while no significant variation of the primary power-law index was found (Murphy, Yaqoob & Terashima 2007); at the end of the campaign the source was again at a low flux state, confirmed by *SUZAKU*, at a flux level of  $\sim 1 \times 10^{-11} \text{ erg cm}^{-2} \text{ s}^{-1}$  (Ptak et al. 2007; Yaqoob et al. 2007) and *CHANDRA*, at flux level of  $\sim 0.3 \times 10^{-11} \text{ erg cm}^{-2} \text{ s}^{-1}$  (its historical minimum flux; Murphy,

Nowak & Marshall 2017). In 2010, NGC 2992 was observed eight times for  $\sim 40$  ks by *XMM-Newton* with a 2–10 keV flux ranging from  $0.3 \times 10^{-11} \text{ erg cm}^{-2} \text{ s}^{-1}$  to  $1.3 \times 10^{-11} \text{ erg cm}^{-2} \text{ s}^{-1}$ . A further 2013 *XMM-Newton* observation caught the source in a higher but still low flux state ( $1.6 \times 10^{-11} \text{ erg cm}^{-2} \text{ s}^{-1}$ ). In 2015, observations performed simultaneously with *Swift* and *NuSTAR* found a 2–10 keV flux of  $6 \times 10^{-11} \text{ erg cm}^{-2} \text{ s}^{-1}$  (Marinucci et al. 2018). The most recent published observations were performed again with *XMM-Newton* in May 2019, when the flux was again at high levels, ranging from  $6.8$  to  $10 \times 10^{-11} \text{ erg cm}^{-2} \text{ s}^{-1}$  (Marinucci et al. 2020).

The optical variability of the source was first explored by Gilli et al. (2000), who noticed that in 1999 the  $H\alpha$  BEL was present again, as it was in early observations of the galaxy by Veron et al. (1980) at the end of the 1970s which led to its first classification as a Seyfert 1.9, in contrast to the Type 2 spectra seen in 1994 by Allen et al. (1999). Later, Trippe et al. (2008) showed that from the beginning of 2006 to the middle of 2007 the source had lost its BEL. Recently Schnorr-Müller et al. (2016) and Guolo et al. (2021) not only showed that the  $H\alpha$  BEL was detectable again but also, for the first time, a very faint  $H\beta$  BEL was claimed to be present.

Besides being a very well-studied galaxy, to the best of our knowledge no study has yet explored the entire X-ray and optical historical emission of NGC 2992, nor attempted to link the behaviour in the two wavelength bands. These are our goals in this paper. The paper is organized as follows: in Section 2 we describe the data collection. The analysis of the data is described in Section 3, while the results are discussed in Section 4. Our conclusions appear in Section 5.

## 2 DATA COLLECTION

This paper results from a careful re-examination of the entire literature on NGC 2992, both X-rays and optical spectra, from its discovery as an X-ray source (Cooke et al. 1978; Ward et al. 1980) and classification as a Seyfert galaxy (Osmer, Smith & Weedman 1974) to the most recent optical and X-ray spectra published to date (Marinucci et al. 2020; Guolo et al. 2021).

### 2.1 Historical X-ray data

The X-ray spectrum of NGC 2992 is very well fitted by an absorbed power law which accounts for most of the X-ray emission. However, the spectrum also presents a narrow iron  $K\alpha$  component at 6.4 keV, which becomes more intense at high flux levels (Yaqoob et al. 2007; Marinucci et al. 2018; Marinucci et al. 2020; see also Section 3.1). We collected the fluxes in the 2–10 keV X-ray band ( $F_{2-10}$ ) and the best-fitting parameters for the absorbed continuum model, namely the power-law continuum photon indexes ( $\Gamma$ )<sup>1</sup> and the absorbed material column densities ( $N_H$ ), as reported by the authors throughout the literature on the source. For the more recent spectra where the narrow Fe  $K\alpha$  is detected we also collected their measured fluxes,  $F(\text{Fe } K\alpha)$ . In the top panel of Fig. 1, we show the historical 2–10 keV light curve. In Table 1, we show the best-fitting continuum model parameters, the Fe  $K\alpha$  fluxes, the observation dates, and references. The  $N_H$  are only accounting for the absorption at the redshift of the source therefore not including Galactic absorption,  $N_{H,\text{Gal}} \approx 5.5 \times 10^{20} \text{ cm}^{-2}$  (Kalberla et al. 2005). Errors in the X-rays parameters correspond to the 90 per cent confidence level for the parameter of interest ( $\Delta\chi^2 = 2.7$ ), as reported by the authors.

<sup>1</sup>The power-law index in the continuum model:  $F(E)\propto E^{-\Gamma}$ .

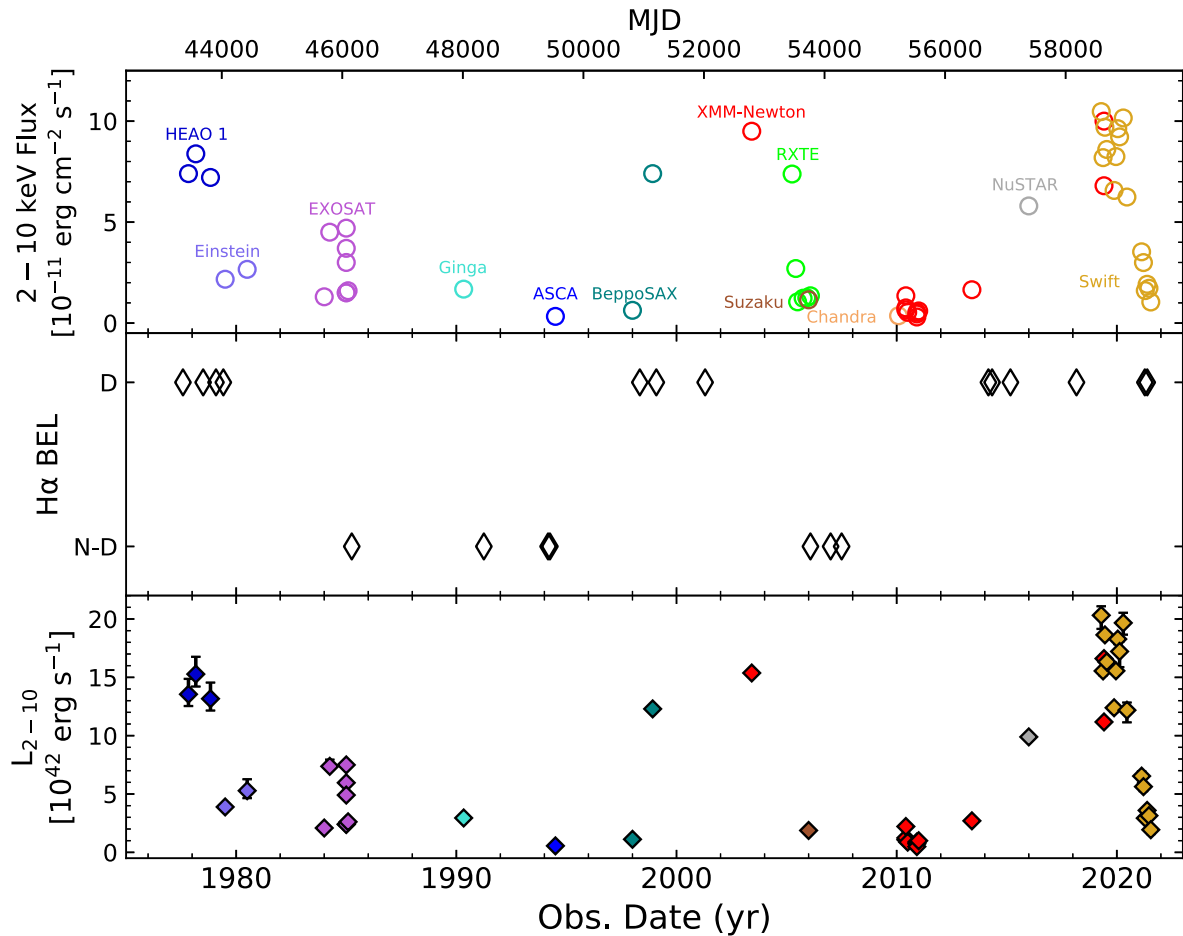


**Figure 1.** Top: historical 2–10 keV light curve of the source. Middle: historical detections (D) and non-detections (N–D) of the broad H $\alpha$  emission line. Bottom: intrinsic (absorption corrected) 2–10 keV Luminosity ( $L_{2-10}$ ) light curve. Each colour represents a distinct X-ray mission, and will be maintained throughout the entire paper. In the  $L_{2-10}$  panel, the points without error bars have errors smaller than  $3 \times 10^{41}$  erg s $^{-1}$ , see Table 1 for the exact values.

For the papers in which the authors reported their uncertainties in another scale, e.g.  $\Delta\chi^2 = 4.6$ , the errors were re-scaled using a PYTHON package (`asymmetric_uncertainties`) for treatment of asymmetric statistical errors derived from confidence levels, which employs a combination of the methods proposed by Barlow (2004) and Possolo, Merktas & Bodnar (2019). The method and a brief discussion on uncertainties can be found in Appendix A. The propagation of the uncertainties for the X-ray derived quantities (see Section 3.1 and Table 1) is also performed with this same method, see Appendix A.

## 2.2 New *Swift* X-ray data

The X-ray Telescope (XRT; Burrows et al. 2005) on-board of the *Neil Gehrels Swift* Observatory started its first monitoring campaign of NGC 2992 in 2019 March, continuing it throughout the entire year (except for the period of early August to late September when the galaxy is in sun-constrained). During 2020 few visits were made, while a second monitoring campaign started in 2021 January; this campaign is still ongoing at the time of this publication. However, in this work, we will limit ourselves to all data taken before 2021 June 15th. All observations were performed in the Photon Counting mode (PC mode; Hill et al. 2004), with exposure times varying between 1 and 2 ks, at a cadence varying between

5 and 7 d. Given that in this work we are only interested in the medium to long-term variability (years/months), not in the short-term (days/weeks) variability, the observations were combined monthly with each resulting spectrum representing the average behaviour of the AGN at the given month. The data in the original cadence may be explored in a future publication by the P.I. of the monitoring campaigns (Middei et al., in preparation). Data were reduced with the task `xrtpipeline` version 0.13.5. As a very nearby source in PC mode, pileup effects may be present, therefore the extractions were made with an annulus aperture that excludes the inner five pixels of the point spread function, using `XSELECT` version 2.4x. The spectral data were re-binned with at least 20 photons per bin using `grppha` version 3.0.0. The auxiliary response files were created with `xrtmkarf` and corrected using the exposure maps, and the standard response matrices `swxpcOto12s6_20130101v014.rmf`. The 0.3–10.0 keV spectra were analysed with `pyXSPEC` version 2.0.3 (Arnaud 1996) by fitting an absorbed power-law model, using again a Galactic absorption,  $N_{\text{H,Gal}} \approx 5.5 \times 10^{20}$  cm $^{-2}$  (Kalberla et al. 2005). Best-fitting  $F_{2-10}$ ,  $N_{\text{H}}$ ,  $\Gamma$ , and their 90 per cent confidence level error are presented in Table 1, while the flux is plotted on the top panel of Fig. 1.

The new *Swift* data shows that the AGN was at its high state during entire 2019 year as well as in the 2020, reaching its maximum observed flux ( $10.4 \times 10^{-11}$  erg cm $^{-2}$  s $^{-1}$ ) in 2019 March. However,

**Table 1.** Historical X-ray data for NGC 2992.

Obs. date <sup>(a)</sup>	Satellite	$F_{2-10}$ <sup>(b)</sup>	$N_{\text{H}}$ <sup>(c)</sup>	$\Gamma$	F(Fe K $\alpha$ ) <sup>(d)</sup>	Reference	$L_{2-10}$ <sup>(e)</sup>
1977 Oct		7.40			–		13.48 <sup>+1.40</sup> <sub>–0.99</sub>
1978 Feb	<i>HEAO 1</i>	8.38	16.0 <sup>+8.0</sup> <sub>–6.0</sub>	1.79 <sup>+0.09</sup> <sub>–0.07</sub>	–	Mushotzky (1982)	15.30 <sup>+1.52</sup> <sub>–1.13</sub>
1978 Oct		7.21			–		13.09 <sup>+1.34</sup> <sub>–0.85</sub>
1979 Jun		2.17	14.3 <sup>+6.0</sup> <sub>–4.0</sub>	1.82 <sup>+0.14</sup> <sub>–0.14</sub>	–	Maccacaro, Perola & Elvis	3.89 <sup>+0.30</sup> <sub>–0.20</sub>
1980 Jun	<i>Einstein</i>	2.66	22.3 <sup>+15.2</sup> <sub>–10.7</sub>	1.92 <sup>+0.47</sup> <sub>–0.47</sub>	–	(1982)	5.25 <sup>+1.01</sup> <sub>–0.64</sub>
1983 Dec		1.30	7.0 <sup>+3.5</sup> <sub>–1.2</sub>	1.46 <sup>+0.23</sup> <sub>–0.16</sub>	–		2.09 <sup>+0.10</sup> <sub>–0.03</sub>
1984 Mar		4.50	7.8 <sup>+6.2</sup> <sub>–1.6</sub>	1.68 <sup>+0.31</sup> <sub>–0.22</sub>	–		7.37 <sup>+0.59</sup> <sub>–0.17</sub>
1984 Dec		4.70	6.0 <sup>+1.7</sup> <sub>–0.6</sub>	1.64 <sup>+0.07</sup> <sub>–0.09</sub>	–		7.50 <sup>+0.18</sup> <sub>–0.07</sub>
1984 Dec	<i>EXOSAT</i>	3.70	7.0 <sup>+1.2</sup> <sub>–0.3</sub>	1.56 <sup>+0.10</sup> <sub>–0.06</sub>	–	Turner & Pounds (1989)	5.96 <sup>+0.12</sup> <sub>–0.03</sub>
1984 Dec		3.00	8.6 <sup>+2.6</sup> <sub>–0.3</sub>	1.48 <sup>+0.15</sup> <sub>–0.11</sub>	–		4.91 <sup>+0.27</sup> <sub>–0.03</sub>
1984 Dec		1.50	6.9 <sup>+7.1</sup> <sub>–1.8</sub>	1.49 <sup>+0.46</sup> <sub>–0.27</sub>	–		2.42 <sup>+0.23</sup> <sub>–0.07</sub>
1984 Dec		1.50	5.6 <sup>+5.2</sup> <sub>–1.2</sub>	1.58 <sup>+0.39</sup> <sub>–0.20</sub>	–		2.39 <sup>+0.19</sup> <sub>–0.05</sub>
1985 Jan		1.60	7.4 <sup>+4.7</sup> <sub>–1.2</sub>	1.67 <sup>+0.31</sup> <sub>–0.17</sub>	–		2.61 <sup>+0.18</sup> <sub>–0.05</sub>
1990 Apr	<i>GINGA</i>	1.68	13.6 <sup>+3.3</sup> <sub>–3.3</sub>	1.64 <sup>+0.08</sup> <sub>–0.08</sub>	–	Nandra & Pounds (1994)	2.94 <sup>+0.12</sup> <sub>–0.12</sub>
1994 Jun	<i>ASCA</i>	0.33	10.1 <sup>+2.7</sup> <sub>–2.3</sub>	1.70 <sup>(f)</sup>	–	Weaver et al. (1996)	0.56 <sup>+0.02</sup> <sub>–0.02</sub>
1997 Dec		0.63	14.0 <sup>+5.0</sup> <sub>–4.0</sub>	1.72 <sup>+0.13</sup> <sub>–0.12</sub>	–		1.12 <sup>+0.07</sup> <sub>–0.06</sub>
1998 Nov	<i>BeppoSAX</i>	7.40	9.0 <sup>+0.3</sup> <sub>–0.3</sub>	1.70 <sup>+0.02</sup> <sub>–0.02</sub>	–	Gilli et al. (2000)	12.29 <sup>+0.05</sup> <sub>–0.05</sub>
2003 May	<i>XMM-Newton</i>	9.50	6.5 <sup>+0.3</sup> <sub>–0.2</sub>	1.83 <sup>+0.06</sup> <sub>–0.04</sub>	–	Shu et al. (2010)	15.37 <sup>+0.07</sup> <sub>–0.05</sub>
2005 Mar		7.38	– <sup>(g)</sup>	1.71 <sup>+0.03</sup> <sub>–0.03</sub>	–		–
2005 May		2.70	–	1.72 <sup>+0.04</sup> <sub>–0.04</sub>	–		–
2005 Jun		1.05	–	1.75 <sup>+0.10</sup> <sub>–0.10</sub>	–		–
2005 Sep	<i>RXTE</i>	1.23	–	1.85 <sup>+0.13</sup> <sub>–0.12</sub>	–	Murphy et al. (2007)	–
2005 Nov		1.25	–	1.96 <sup>+0.12</sup> <sub>–0.11</sub>	–		–
2006 Jan		1.35	–	1.76 <sup>+0.08</sup> <sub>–0.08</sub>	–		–
2005 Dec	<i>SUZAKU</i>	1.15	8.0 <sup>+0.6</sup> <sub>–0.4</sub>	1.57 <sup>+0.05</sup> <sub>–0.03</sub>	3.99 <sup>+0.80</sup> <sub>–0.80</sub>	Yaqoob et al. (2007)	1.88 <sup>+0.01</sup> <sub>–0.01</sub>
2010 Jan	<i>CHANDRA</i>	0.36	–	–	–	Murphy et al. (2017)	–
2010 May		0.65	9.2 <sup>+1.0</sup> <sub>–1.0</sub>	1.67 <sup>+0.05</sup> <sub>–0.05</sub>	3.51 <sup>+0.35</sup> <sub>–0.35</sub>		1.08 <sup>+0.01</sup> <sub>–0.01</sub>
2010 May		0.75	8.6 <sup>+1.0</sup> <sub>–1.0</sub>	1.64 <sup>+0.04</sup> <sub>–0.04</sub>	2.96 <sup>+0.42</sup> <sub>–0.42</sub>		1.24 <sup>+0.02</sup> <sub>–0.01</sub>
2010 May		1.35	8.4 <sup>+1.0</sup> <sub>–1.0</sub>	1.61 <sup>+0.04</sup> <sub>–0.04</sub>	4.49 <sup>+0.48</sup> <sub>–0.48</sub>		2.22 <sup>+0.03</sup> <sub>–0.03</sub>
2010 Jun	<i>XMM-Newton</i>	0.53	8.5 <sup>+1.0</sup> <sub>–1.0</sub>	1.67 <sup>+0.05</sup> <sub>–0.05</sub>	3.69 <sup>+0.32</sup> <sub>–0.32</sub>		0.87 <sup>+0.01</sup> <sub>–0.01</sub>
2010 Nov		0.54	8.0 <sup>+1.0</sup> <sub>–1.0</sub>	1.67 <sup>+0.05</sup> <sub>–0.05</sub>	3.64 <sup>+0.34</sup> <sub>–0.34</sub>	Marinucci et al. (2018)	0.88 <sup>+0.01</sup> <sub>–0.01</sub>
2010 Nov		0.45	8.0 <sup>+1.0</sup> <sub>–1.0</sub>	1.70 <sup>+0.06</sup> <sub>–0.06</sub>	3.70 <sup>+0.35</sup> <sub>–0.35</sub>		0.74 <sup>+0.01</sup> <sub>–0.01</sub>
2010 Nov		0.30	8.1 <sup>+1.0</sup> <sub>–1.0</sub>	1.71 <sup>+0.09</sup> <sub>–0.09</sub>	3.19 <sup>+0.32</sup> <sub>–0.32</sub>		0.49 <sup>+0.01</sup> <sub>–0.01</sub>
2010 Dec		0.60	9.0 <sup>+1.0</sup> <sub>–1.0</sub>	1.68 <sup>+0.04</sup> <sub>–0.04</sub>	3.00 <sup>+0.37</sup> <sub>–0.37</sub>		1.00 <sup>+0.01</sup> <sub>–0.01</sub>
2013 May		1.65	8.1 <sup>+1.0</sup> <sub>–1.0</sub>	1.63 <sup>+0.06</sup> <sub>–0.06</sub>	5.66 <sup>+1.12</sup> <sub>–1.12</sub>		2.70 <sup>+0.03</sup> <sub>–0.03</sub>
2015 Dec	<i>NuSTAR</i>	5.80	11.0 <sup>+2.0</sup> <sub>–2.0</sub>	1.72 <sup>+0.03</sup> <sub>–0.03</sub>	8.68 <sup>+1.92</sup> <sub>–1.92</sub>		9.89 <sup>+0.26</sup> <sub>–0.24</sub>
2019 May	<i>XMM-Newton</i>	10.00	9.0 <sup>+1.6</sup> <sub>–1.6</sub>	1.68 <sup>+0.10</sup> <sub>–0.10</sub>	12.96 <sup>+1.60</sup> <sub>–1.60</sub>		16.59 <sup>+0.34</sup> <sub>–0.34</sub>
2019 May		6.80	8.5 <sup>+1.6</sup> <sub>–1.6</sub>	1.63 <sup>+0.06</sup> <sub>–0.06</sub>	12.96 <sup>+1.60</sup> <sub>–1.60</sub>	Marinucci et al. (2020)	11.18 <sup>+0.23</sup> <sub>–0.22</sub>
2019 Mar		10.47 <sup>+0.38</sup> <sub>–0.50</sub>	9.3 <sup>+1.6</sup> <sub>–1.4</sub>	1.77 <sup>+0.16</sup> <sub>–0.15</sub>	–		20.32 <sup>+0.77</sup> <sub>–1.16</sub>
2019 Apr		8.19 <sup>+0.16</sup> <sub>–0.20</sub>	7.9 <sup>+0.8</sup> <sub>–0.7</sub>	1.50 <sup>+0.08</sup> <sub>–0.08</sub>	–		15.55 <sup>+0.30</sup> <sub>–0.38</sub>
2019 May		9.70 <sup>+0.12</sup> <sub>–0.12</sub>	8.9 <sup>+0.5</sup> <sub>–0.5</sub>	1.63 <sup>+0.05</sup> <sub>–0.05</sub>	–		18.64 <sup>+0.21</sup> <sub>–0.19</sub>
2019 Jun		8.60 <sup>+0.15</sup> <sub>–0.20</sub>	7.9 <sup>+0.7</sup> <sub>–0.7</sub>	1.51 <sup>+0.07</sup> <sub>–0.07</sub>	–		16.33 <sup>+0.31</sup> <sub>–0.36</sub>
2019 Oct		6.57 <sup>+0.13</sup> <sub>–0.22</sub>	7.3 <sup>+1.0</sup> <sub>–0.9</sub>	1.45 <sup>+0.09</sup> <sub>–0.09</sub>	–		12.39 <sup>+0.31</sup> <sub>–0.37</sub>
2019 Nov		8.24 <sup>+0.14</sup> <sub>–0.17</sub>	7.4 <sup>+0.5</sup> <sub>–0.5</sub>	1.43 <sup>+0.06</sup> <sub>–0.06</sub>	–		15.56 <sup>+0.28</sup> <sub>–0.28</sub>
2019 Dec	<i>Swift</i>	9.63 <sup>+0.20</sup> <sub>–0.24</sub>	7.8 <sup>+0.6</sup> <sub>–0.6</sub>	1.53 <sup>+0.07</sup> <sub>–0.06</sub>	–	This Work	18.28 <sup>+0.30</sup> <sub>–0.43</sub>
2020 Jan		9.22 <sup>+0.72</sup> <sub>–0.57</sub>	5.7 <sup>+2.2</sup> <sub>–1.9</sub>	1.49 <sup>+0.23</sup> <sub>–0.22</sub>	–		17.22 <sup>+0.82</sup> <sub>–1.34</sub>
2020 Mar		10.16 <sup>+0.40</sup> <sub>–0.60</sub>	9.6 <sup>+2.2</sup> <sub>–1.9</sub>	1.69 <sup>+0.20</sup> <sub>–0.18</sub>	–		19.67 <sup>+0.87</sup> <sub>–1.01</sub>
2020 May		6.24 <sup>+0.38</sup> <sub>–0.57</sub>	10.7 <sup>+3.1</sup> <sub>–2.7</sub>	1.68 <sup>+0.29</sup> <sub>–0.27</sub>	–		12.18 <sup>+0.66</sup> <sub>–1.04</sub>
2021 Jan		3.53 <sup>+0.19</sup> <sub>–0.27</sub>	5.5 <sup>+2.1</sup> <sub>–1.8</sub>	1.24 <sup>+0.22</sup> <sub>–0.21</sub>	–		6.54 <sup>+0.41</sup> <sub>–0.58</sub>
2021 Feb		3.00 <sup>+0.12</sup> <sub>–0.17</sub>	7.0 <sup>+1.6</sup> <sub>–1.4</sub>	1.40 <sup>+0.16</sup> <sub>–0.15</sub>	–		5.63 <sup>+0.20</sup> <sub>–0.39</sub>
2021 Mar		1.61 <sup>+0.10</sup> <sub>–0.12</sub>	3.3 <sup>+1.6</sup> <sub>–1.2</sub>	1.11 <sup>+0.19</sup> <sub>–0.17</sub>	–		2.93 <sup>+0.14</sup> <sub>–0.20</sub>
2021 Apr		1.92 <sup>+0.09</sup> <sub>–0.11</sub>	6.2 <sup>+1.6</sup> <sub>–1.4</sub>	1.44 <sup>+0.18</sup> <sub>–0.17</sub>	–		3.59 <sup>+0.17</sup> <sub>–0.18</sub>
2021 May		1.72 <sup>+0.10</sup> <sub>–0.13</sub>	3.6 <sup>+1.7</sup> <sub>–1.3</sub>	1.10 <sup>+0.19</sup> <sub>–0.17</sub>	–		3.14 <sup>+0.19</sup> <sub>–0.22</sub>
2021 Jun		1.04 <sup>+0.08</sup> <sub>–0.21</sub>	5.2 <sup>+4.4</sup> <sub>–3.7</sub>	1.44 <sup>+0.50</sup> <sub>–0.46</sub>	–		1.94 <sup>+0.14</sup> <sub>–0.37</sub>

Note. <sup>(a)</sup> yyyy/mm. <sup>(b)</sup> in units of  $10^{-11}$  erg  $\text{cm}^{-2}$   $\text{s}^{-1}$ . <sup>(c)</sup> In units of  $10^{21}$   $\text{cm}^{-2}$ . <sup>(d)</sup> In units of  $10^{-14}$  erg  $\text{cm}^{-2}$   $\text{s}^{-1}$ . <sup>(e)</sup> Absorption corrected, in units of  $10^{42}$  erg  $\text{s}^{-1}$ . <sup>(f)</sup> The value was frozen in the model fitting; therefore it was excluded in the analyses of the  $\Gamma$  parameter variability of Section 3.1. <sup>(g)</sup> Values not provided by the authors.

**Table 2.** Historical broad H $\alpha$  line and Seyfert Type classification for NGC 2992.

Obs. date <sup>(a)</sup>	H $\alpha$ BEL <sup>(b)</sup>	Reference
1977 Jul	D	Ward et al. (1980)
< 1978	D	Veron et al. (1980)
1979 Jan	D	Shuder (1980)
1979 May	D	Durret & Bergeron (1988)
1985 Mar	N-D	Busko & Steiner (1990)
1991 Mar	N-D	Marquez et al. (1998)
1994 Feb	N-D	Veilleux et al. (2001)
1994 Mar	N-D	Allen et al. (1999)
1998 Apr	D	García-Lorenzo et al. (2001)
1999 Jan	D	Gilli et al. (2000)
2001 Mar	D	Stoklasová et al. (2009)
2006 Jan	N-D	
2006 Dec	N-D	Trippe et al. (2008)
2007 Jun	N-D	
2014 Feb	D	Schnorr-Müller et al. (2016)
2014 Apr	D	Dopita et al. (2015)
2015 Feb	D	Mingozzi et al. (2019)
2018 Feb	D	Guolo et al. (2021)
2021 Mar	D	
2021 Apr	D	This Work

Note. <sup>(a)</sup> yyyy/mm. <sup>(b)</sup> Whether the H $\alpha$  BEL was Detected (D) or Not-Detected (N-D).

early 2021 data shows the AGN constantly declining its flux since January ( $3 \times 10^{-11}$  erg cm $^{-2}$  s $^{-1}$ ), with March–May observations having a flux of  $1.5\text{--}2 \times 10^{-11}$  erg cm $^{-2}$  s $^{-1}$  comparable with 2013 *XMM-Newton* data (Marinucci et al. 2018), while June data reaches an even lower flux value of  $1 \times 10^{-11}$  erg cm $^{-2}$  s $^{-1}$ , showing that the AGN is again transitioning to its low flux state.

### 2.3 Historical optical spectra

To access the historical presence or absence of H $\alpha$  BEL and the galaxy optical classification, we reviewed all papers that report optical spectra of the galaxy. As most of these spectra are not available to allow intercalibration and measurement of the BELs flux variability, we restrict ourselves to a binary classification of the H $\alpha$  BEL, i.e. whether the component was undoubtedly detected (D) or not-detected (N-D) by the authors. We do so by searching for a detection or non-detection claim in the original text and by visually inspecting the published spectra. In the middle panel of Fig. 1, we show the H $\alpha$  BEL detection history. In Table 2, we show the observation dates, the references and the Seyfert type at the time.

In summary: the first spectra of the galaxy in the '70s (Shuder 1980; Ward et al. 1980; Veron et al. 1980; Durret & Bergeron 1988) detected only H $\alpha$  broad components, with no counterpart in H $\beta$ , resulting in its original classification as a Seyfert 1.9 galaxy. Throughout mid '80s to the mid '90s several authors have reported that the BEL H $\alpha$  was not detectable anymore (Busko & Steiner 1990; Allen et al. 1999; Marquez et al. 1998; Veilleux, Shopbell & Miller 2001), changing its classification to Seyfert 2 Type. However, the broad component was detected again from the end of the '90s to the beginning of the 2000s (Gilli et al. 2000; García-Lorenzo, Arribas & Mediavilla 2001; Stoklasová et al. 2009). Later, Trippe et al. (2008) performed an 18 months long monitoring campaign from the beginning of 2006 to mid-2007 that revealed the H $\alpha$  BEL component was missing again, throughout the entire campaign. More recent observations have shown that the galaxy has regained the broad H $\alpha$  component (Dopita et al. 2015; Schnorr-Müller et al. 2016; Mingozzi

et al. 2019), and for the first time, an H $\beta$  BEL was unambiguously detected, in late 2018, by Guolo et al. (2021), therefore changing its classification to a 1.8 Type Seyfert galaxy.

### 2.4 Modern optical spectra

For four of the six most recent published spectra of NGC 2992, we were able to apply methods of flux inter-calibration that have been developed for reverberation mapping studies (van Groninge & Wanders 1992; Peterson 1993; Peterson et al. 1995; Fausnaugh 2017) and measure the intrinsic flux variability of the BELs. The spectra are from:

(i) Trippe et al. (2008) and taken in December of 2006 in the Cerro Tololo Inter-American Observatory; the spectrum was obtained by private communication with one of the authors. Spectra were observed using two different settings: one with a grating with a resolution of 4.3 Å ( $R = \lambda/\Delta\lambda \sim 1000$ ) to take blue spectra from approximately 3660–5440Å, and the other with a resolution of 3.1 Å ( $R \sim 3000$ ) to take red spectra from approximately 5650–6970Å;

(ii) Dopita et al. (2015) as part of the Siding Spring Southern Seyfert Spectroscopic Snapshot Survey (S7), taken in April of 2014 and publicly available at the S7 survey website. The spectra covers the waveband 3400–7100Å with a high resolution of  $R = 7000$  in the redder (5300–7100 Å), and  $R = 3000$  in the bluer (3400–5700 Å) wavelengths;

(iii) Mingozzi et al. (2019) as part of the Measuring AGN Under MUSE Microscope (MAGNUM) survey using the Multi-Unit Spectroscopic Explorer (MUSE) at the very large telescope (VLT) and taken in February of 2015; the spectral data cube is publicly available at the VLT archive; its spectral resolution goes from 1750 at 4650 Å to 3750 at 9300 Å;

(iv) Guolo et al. (2021) taken using the Gemini Multi-Object Spectrographs (GMOS) at the Gemini South Telescope in February of 2018. The observed spectra covered a range from 4075 to 7285 Å with and a spectral resolution of  $R \sim 5000$  at H $\alpha$ .

The analyses of *Swift* data signalled that the AGN flux was declining again to its fainter state while this publication was being written, motivating us to obtain new optical spectra. We proposed and obtained Director Discretionary Time (DDT) at the following Telescopes:

(i) Southern Astrophysical Research Telescope (SOAR), using the SOAR Integral Field Spectrograph (SIFS; Lepine et al. 2003) instrument, on the night of 2021 08 March. Three 20 min exposures were made using a 700 l/mm grating, covering from 4500 to 7300 Å with an  $R \sim 4200$  spectral resolution;

(ii) The Gemini South Telescope, using the GMOS, on the night of 2021 17 April. Two 10 min exposures were made using the same instrumental configuration and having the same spectral coverage and resolution as in Guolo et al. (2021).

The standard reduction processes were performed in the two spectra data cubes: bias subtraction, flatfielding, trimming, wavelength calibration, telluric emission subtraction, relative flux calibration, the building of the data cubes, and finally the combination of the distinct exposures.

The inter-calibration, aperture or seeing corrections, and the process for emission line fitting of the six spectra will be presented in Section 3.2. It is important to note the large number of data points collected: 56 in the X-rays (49 with  $N_{\text{H}}$  and  $\Gamma$  values) and 20 in the optical, which allow us to have a quasi-contemporaneous X-ray

**Table 3.** Black hole mass estimates for NGC 2992. Uncertainties are at 68 per cent ( $1\sigma$ ) confidence level.

$M_{\text{BH}} (M_{\odot})$	Method	References
$5.2 \times 10^7$	$M_{\text{BH}} - \sigma_*$ (Tremaine et al. 2002)	Woo & Urry (2002) ( $\sigma_* = 158 \text{ km s}^{-1}$ )
$4.8_{-2.4}^{+3.9} \times 10^7$	$M_{\text{BH}} - \sigma_*$ (Gültekin et al. 2009)	Nelson & Whittle (1995) ( $\sigma_* = 158 \pm 13 \text{ km s}^{-1}$ )
$3.0_{-1.5}^{+5.5} \times 10^7$	$\sigma_{\text{rms}}^2 - M_{\text{BH}}$ (Ponti et al. 2012)	Marinucci et al. (2020)
$1.2_{-0.7}^{+1.5} \times 10^7$		This Work (2006 spectra)
$1.3_{-1.0}^{+3.8} \times 10^7$		This Work (2014 spectra)
$3.5_{-2.5}^{+9.1} \times 10^7$	$M_{\text{SE}}(\sigma_{H\beta}, L_{H\beta})$ (Dalla Bontà et al. 2020)	This Work (2015 spectra)
$2.4_{-1.4}^{+3.2} \times 10^7$		This Work (2018 spectra)
$2.5_{-1.3}^{+2.7} \times 10^7$		This Work (03/2021 spectra)
$2.2_{-1.1}^{+2.3} \times 10^7$		This Work (04/2021 spectra)

measurement for each optical spectrum, within less than 1 yr for most, and less than 2 yr for all of them; see Fig. 1.

## 2.5 Estimates of the black hole mass and luminosity distance

Precise black hole mass and luminosity distance measurements are essential for the energetic calibrations and scaling to come. Using stellar velocity dispersion measurements of  $\sigma_* = 158 \text{ km s}^{-1}$ , Woo & Urry (2002) estimated the black hole mass of NGC 2992 to be  $5.2 \times 10^7 M_{\odot}$  by applying the Tremaine et al. (2002)  $M_{\text{BH}} - \sigma_*$  relation. The value obtained from the Gültekin et al. (2009)  $M_{\text{BH}} - \sigma_*$  relation is  $M_{\text{BH}} = 4.8_{-2.4}^{+3.9} \times 10^7 M_{\odot}$ , using a bulge stellar velocity dispersion  $\sigma_* = 158 \pm 13 \text{ km s}^{-1}$  (Nelson & Whittle 1995). From the normalized excess variance  $\sigma_{\text{rms}}^2$  in the 2–10 keV band and assuming the  $\sigma_{\text{rms}}^2 - M_{\text{BH}}$  correlation from Ponti et al. (2012), Marinucci et al. (2020) reported an  $M_{\text{BH}} = 3.0_{-1.5}^{+5.5} \times 10^7 M_{\odot}$ . Furthermore, we also estimate the SMBH mass using the emission line measurements to be described in Section 3.2.2, by using single-epoch (SE)  $M_{\text{BH}}$  estimates. We applied Dalla Bontà et al. (2020)  $M_{\text{SE}}(\sigma_{H\beta}, L_{H\beta})$  relation using all six modern spectra (Section 2.4). We corrected the spectra for extinction effects using the measured Balmer decrements and assuming Calzetti et al. (2000) extinction law. We obtained the following values for  $M_{\text{BH}}$ :  $1.3_{-1.0}^{+3.8} \times 10^7 M_{\odot}$ ,  $3.5_{-2.5}^{+9.1} \times 10^7 M_{\odot}$ ,  $2.4_{-1.4}^{+3.2} \times 10^7 M_{\odot}$ , and  $2.2_{-1.1}^{+2.3} \times 10^7 M_{\odot}$ , respectively for 2014, 2015, 2018, and 2021 April spectra. As the  $H\beta$  BEL was not detected in the 2006 and 2021 March spectra, we use the  $H\alpha$  BEL, assuming a Balmer decrement of nine (see Section 3.2.3). We obtained, respectively,  $1.2_{-0.7}^{+1.5} \times 10^7 M_{\odot}$  and  $2.5_{-1.3}^{+2.7} \times 10^7 M_{\odot}$ . In Table 3 we summarize the estimated values, although the distinct methods results in distinct values, they are all within the  $1 - 6 \times 10^7 M_{\odot}$  range.

Theureau et al. (2007) found a recession velocity of  $2657 \text{ km s}^{-1}$  for NGC 2992 (already corrected for peculiar motions), which assuming a cosmology with  $H_0 = 70 \text{ km s}^{-1} \text{ Mpc}^{-1}$ , translates to a luminosity distance to NGC 2992 equals to 38 Mpc.

## 3 DATA ANALYSES

### 3.1 X-ray variability

In the scenario where the CL events are caused by variable absorption, two natural consequences are an anticorrelation between  $N_{\text{H}}$  and  $F_{2-10}$  and a constant intrinsic (absorption corrected) luminosity. In the top panel of Fig. 2 we show  $\log N_{\text{H}}$  as function of  $F_{2-10}$ : no clear anticorrelation can be seen. The Spearman rank correlation coefficient ( $r_s$ ) for the two variables and its correspondent  $p_{\text{value}}$  are  $r_s = 0.02_{-0.11}^{+0.10}$  and  $p_{\text{value}} = 0.93_{-0.59}^{+0.07}$ , while the best-fitting constant value is  $N_{\text{H}} = 21.93_{-0.03}^{+0.03}$ , where the errors correspond to 90 per cent confidence level measured by performing a thousand Monte Carlo iterations (see details in Appendix A).

We can therefore conclude that although there were some variations in the column density, it is not anticorrelated with the X-ray flux as seen in variable absorption CL-AGNs (e.g. Puccetti et al. 2007; Bianchi et al. 2009). A further confirmation that the absorption is not the main factor responsible for the behaviour of the source can be seen by the intrinsic (i.e. absorption corrected) rest-frame luminosity ( $L_{2-10}$ ). The measured  $L_{2-10}$  values, for each observation in which an  $N_{\text{H}}$  value is provided, are presented in Table 1. The values range from  $4.9 \times 10^{41} \text{ erg s}^{-1}$  to  $\sim 2.0 \times 10^{43} \text{ erg s}^{-1}$ . The  $L_{2-10}$  light curve is shown in the bottom panel of Fig. 1, and it has the same behaviour as  $F_{2-10}$  confirming that the variations are intrinsic and not due to changes in absorption.

The Spearman rank correlation test shows that there is no monotonic correlation between the photon index  $\Gamma$  and the X-rays flux (or luminosity) for NGC 2992 (middle panel of Fig. 2). The values found were  $r_s = 0.02_{-0.12}^{+0.12}$  and  $p_{\text{value}} = 0.90_{-0.66}^{+0.10}$ . The existence of a correlation between luminosity and photon index in AGNs is in fact debatable, and several contradictory results have been presented in the last years. While Dai et al. (2004) reported the existence of a positive correlation, other works found none (e.g. Winter et al. 2009) or a negative correlation (e.g. Corral et al. 2011). A ‘V’ shape for the  $\Gamma$  versus  $L_{\text{Edd}}$  relation for NGC 2992 was claimed by Liu et al. (2019); the authors interpreted this as a change in accretion mode, similar to the ones that occur in stellar-mass X-ray binaries, e.g. Qiao & Liu (2013). We argue here that their finding is due to selection effects, as the authors only used data from 2003 to 2013. When the entire historical data of the source is shown (Fig. 2), this effect is not seen. In contrast, there is a positive correlation between  $F_{2-10}$  and the flux of the Fe  $K\alpha$  line, with  $r_s = 0.69_{-0.11}^{+0.07}$  and  $p_{\text{value}} = 0.01_{-0.01}^{+0.03}$ . Fitting the data by assuming a relation of the type:

$$\log F(\text{Fe } K\alpha) = \alpha + \beta \log F_{2-10}, \quad (1)$$

we obtained a slope of  $\beta = 0.39 \pm 0.04$ . As the iron  $K\alpha$  line is created by reprocessing of the primary X-ray continuum, a tight correlation between the flux of the line and that of the continuum is expected. For large samples of AGNs Ricci et al. (2014), found  $\beta = 0.89 \pm 0.04$ , while Shu et al. (2010) found  $\beta = 0.86 \pm 0.01$ . However, NGC 2992 seems to be one of a few objects where this correlation is found in a single object, though with a lower slope than the ones found in the general AGN population.

### 3.2 Modern optical spectra analyses

In this section, we explore the flux variability of the BELs using four of the six most recent spectra, namely from 2006 December, 2014 April, 2015 February, 2018 February, 2021 March, 2021 April (see

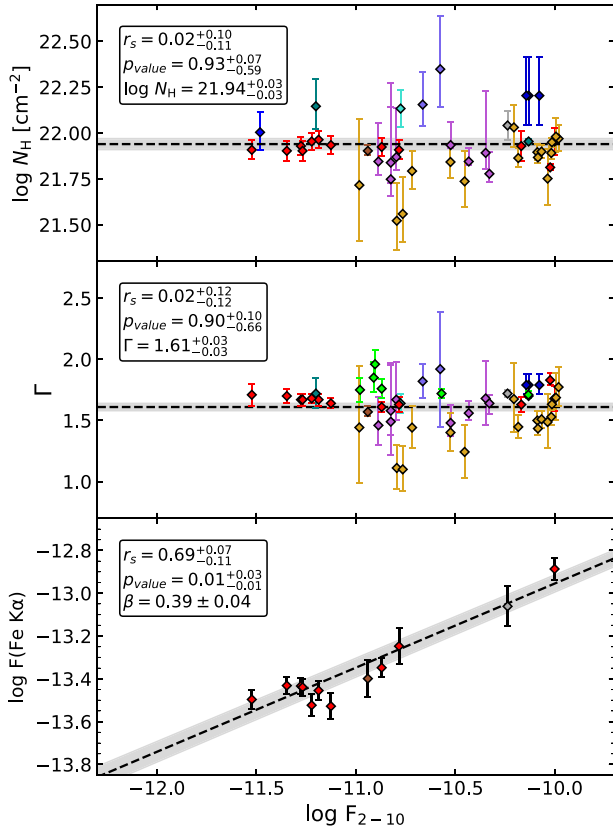


**Figure 2.** Best-fitting parameters  $N_H$  (top panel) and  $\Gamma$  (middle panel) for an absorbed power-law continuum model as function of the 2–10 keV Flux. The left top boxes show the Spearman rank correlation coefficient ( $r_s$ ) for the two variables and its corresponding  $p$ -value, as well as the best-fitting constant values. Fe  $K\alpha$  flux as function as function of the 2–10 keV flux. The left top box show the Spearman rank correlation coefficient ( $r_s$ ) for the two variables and its corresponding  $p$ -value,  $\beta$  is the slope of the best-fitting line (see equation 1).

Table 2). Uncertainties derived from any optical observation are at 68 per cent ( $1\sigma$ ) confidence level.

### 3.2.1 Absolute calibration of the spectra

Even under the best conditions, which are not often realized, flux calibration of ground-based spectrophotometry is no better than  $\approx 5$  per cent, which is insufficient for detailed comparisons of variable spectra. Thus the standard technique of flux calibration, through

**Table 4.** Modern optical spectra. Point-source scale factor ( $\varphi$ ) is measured using Peterson et al. (1995) algorithm, the errors in  $\varphi$  represents the uncertainty in the centring of the virtual apertures. Uncertainties are at 68 per cent ( $1\sigma$ ) confidence level.

Obs. Date	Aperture	Point-Source Scale Factor $\varphi$	$F(H\alpha)^a$	$FWHM(H\alpha)^b$	$F(H\beta)^a$	$F(H\alpha)/F(H\beta)$
2006 Dec	Slit (width = 2.0 arcsec)	$0.734 \pm 0.063$	$\leq 4.4$	$2733 \pm 55$	–	–
2014 Apr	Circular ( $r = 2.8$ arcsec)	$0.972 \pm 0.025$	$27.5 \pm 1.4$	$2002 \pm 28$	$3.6 \pm 2.6$	$7.6 \pm 2.8$
2015 Feb	Circular ( $r = 3.0$ arcsec)	1.000	$33.8 \pm 1.5$	$2313 \pm 17$	$3.3 \pm 2.2$	$10.1 \pm 3.3$
2018 Feb	Circular ( $r = 3.0$ arcsec)	$0.973 \pm 0.013$	$43.8 \pm 2.2$	$2016 \pm 13$	$4.9 \pm 1.4$	$8.8 \pm 1.7$
2021 Mar	Circular ( $r = 3.0$ arcsec)	$1.000 \pm 0.012$	$25.4 \pm 2.0$	$2209 \pm 15$	$\leq 3.1$	$\geq 8.2$
2021 Apr	Circular ( $r = 2.0$ arcsec)	$0.862 \pm 0.009$	$18.5 \pm 0.5$	$2225 \pm 5$	$1.7 \pm 0.1$	$10.3 \pm 0.9$

<sup>a</sup> $10^{-13}$  erg  $\text{cm}^{-2}$   $\text{s}^{-1}$ .

<sup>b</sup>km  $\text{s}^{-1}$ .

comparison with stars of known spectral energy distribution, is not good enough for the study of AGN variability. Instead, we use the fluxes of the narrow emission lines known to be non-variable on time-scales of tens of years in most AGN. Consequently, the bright narrow emission lines can be adopted as internal calibrators for scaling AGN spectra (Peterson 1993). We assume that the flux of the [O III]  $\lambda 5007$  line remains constant during the interval covered by these spectra.

We extracted the spectra using virtual apertures from the original data, making them as similar as possible to each other in the data cubes, as shown in Table 4. The scaling of the extracted spectra was carried out using a refinement of the method of van Groningen & Wanders (1992), implemented as a Python package (MAPSPEC) by Fausnaugh (2017). This method allows us to obtain a homogeneous set of spectra with the same wavelength solution, same spectral resolution (at  $\sim 6300\text{\AA}$ ), and the same [O III]  $\lambda 5007$  flux value.

### 3.2.2 Stellar component subtraction and emission-line fitting

We subtracted the host galaxy stellar continuum fitted using the STARLIGHT (Cid Fernandes et al. 2005) full spectra fitting code, using a base of 45 simple stellar population (SSP) spectra, with 15 ages (from 1 Myr to 13 Gyr) and 3 metallicities (0.2, 1.0, and 2.5  $Z_\odot$ ). The emission line fitting was performed using the IFSCUBE package (Ruschel-Dutra & de Oliveira 2020). The code employs sequential least square programming and allows multiple components with physically motivated constraints. In order to measure the BEL fluxes, the narrow emission components must be separated from the broad components. This process is not straightforward due to the fact the BELs are blended with the narrow lines, for both  $H\alpha$  and  $H\beta$ .

The narrow line subtraction was performed in two steps. First, we fitted the narrow and broad  $H\alpha$  and  $H\beta$  simultaneously. For the narrow lines, we created a template comprised of two Gaussian components that were based on the [S II]  $\lambda 6716$  profile. This template was used to fit the [N II] and narrow  $H\alpha$  and  $H\beta$  lines by adjusting its flux scaling factor only. The fits to the broad lines were subtracted from the spectra, isolating the narrow emission; we then re-fitted the narrow lines assuming the H I and [N II] lines have the same velocity dispersion and redshift and we set the flux of [N II]  $\lambda 6583$  line as 2.96 times that of the [N II]  $\lambda 6548$  line, in accordance with the ratio of their transition probabilities (Osterbrock & Ferland 2006), while the  $H\alpha$  and [N II]  $\lambda 6583$  fluxes were free parameters in the fit. Finally, we subtracted the resulting narrow lines from the original spectrum and re-fit only broad lines using three Gaussian components, in order to account for the known non-Gaussian profiles of the BEL. The errors were taken as the standard deviations of one hundred Monte Carlo iterations. The resulting fits for the four spectra are shown in Fig. 3.

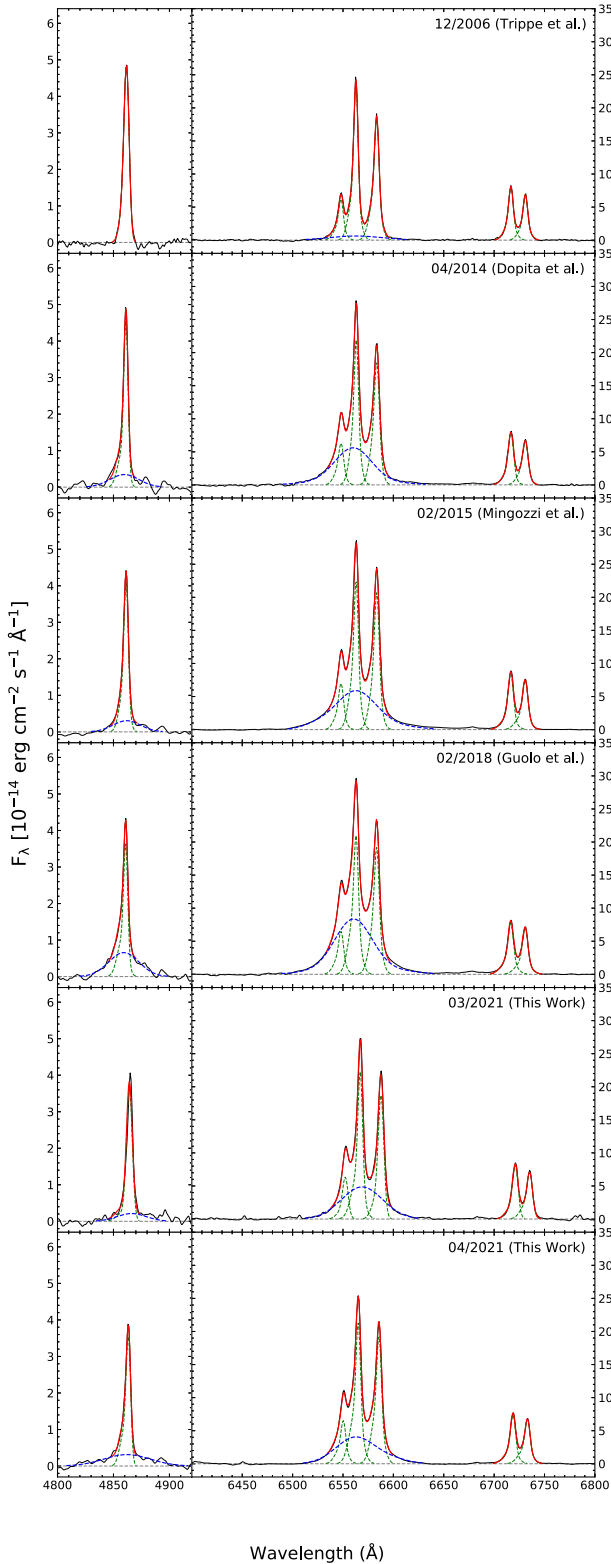


**Figure 3.** Fit of the emission lines for the modern optical spectra. From top to bottom: 2006 December (Trippe et al. 2008), 2014 April (Dopita et al. 2015), 2015 February (Mingozzi et al. 2019), 2018 February (Guolo et al. 2021), and the new spectra from 2021 March and April. Scaled observed spectra (black), narrow components (green), broad components (blue), and total model (red) are shown. Left-hand panels show the H $\beta$  lines, while right ones show the H $\alpha$ , [N II], and [S II] lines.

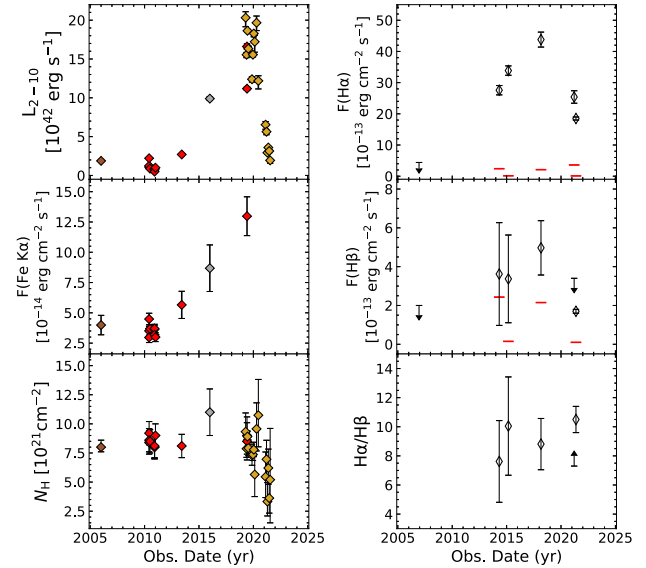


**Figure 4.** X-ray (left) and optical (right) properties from 2005 to 2020. From top to bottom in the X-ray panels: intrinsic 2–10 keV Luminosity ( $L_{2-10}$ ), narrow Fe K $\alpha$  line flux, and the column density ( $N_{\text{H}}$ ). From top to bottom in the optical panels: flux of the H $\alpha$  BEL, the flux of the H $\beta$  BEL, and the Balmer decrement (H $\alpha$ /H $\beta$ ). In the optical panels, the red lines represent a lower limit for the detection of the lines, being measured as the flux of a line with a S/N equals to five. In the cases in which the emission lines are not detected above this S/N, the upper limits are shown.

### 3.2.3 Inter-calibration of the spectral data

The fluxes measured in the scaled spectrum described in the previous sections were corrected for aperture and distinct seeing effects, because while the BLR is effectively a point-like source, the NLR is an extended one. Consequently, the measured NLR flux depends on the size of the spectrograph’s entrance aperture and the observations seeing (see Peterson et al. 1995, for a detailed discussion). In order to correct our fluxes for these effects, we determined a point-source correction factor ( $\varphi$ ), which was measured using the procedure described in Peterson et al. (1995). The  $\varphi$  value represents the differences in the amount of light from the NLR with respect to the amount of light from the BLR for each observation, it is normalized using the largest aperture ( $\varphi \equiv 1.0$ , for 2015 April spectrum). Then the scaled inter-calibrated and aperture or seeing corrected BEL fluxes were measured as follows:

$$F(H\alpha) = \varphi \cdot F_{\lambda 5007} \left[ \frac{F(H\alpha)}{F([\text{O III}]\lambda 5007)} \right]_{\text{obs}}, \quad (2)$$

where  $F_{\lambda 5007}$  is the scaling absolute flux in the [O III] $\lambda 5007$  line, described in Section 3.2.1, and the value in brackets is the broad H $\alpha$  to [O III] $\lambda 5007$  measured flux ratio for each spectrum as described in Section 3.2.2. The same procedure was applied to H $\beta$  BEL. The BEL H $\alpha$  and H $\beta$  fluxes and the Balmer decrements (H $\alpha$ /H $\beta$ ) are shown in Table 4 and in the right-hand panels of Fig. 4. In order to consider a valid BEL detection we required a signal-to-noise ratio (S/N) greater than five; if the BEL is not detected above this level we report the upper limit flux. In the 2006 December spectrum, the H $\alpha$  BEL is not unambiguously detected (which leads to its classification as a Seyfert 2), and if it is indeed present, it is very faint, with an upper limit flux of  $4.4 \times 10^{-13} \text{ erg cm}^{-2} \text{ s}^{-1}$ . From 2014 to 2018 the broad H $\alpha$  flux increases from  $\sim 28 \times 10^{-13} \text{ erg cm}^{-2} \text{ s}^{-1}$  to  $\sim 44 \times 10^{-13} \text{ erg cm}^{-2} \text{ s}^{-1}$ . The new 2021 spectra, however, show



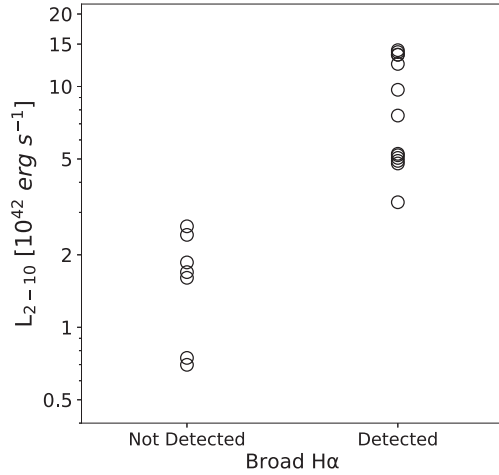


**Figure 5.** Interpolated intrinsic 2–10 keV X-ray luminosity ( $L_{2-10}$ ) for each optical spectrum as function of the detection or non-detection of the  $H\alpha$  BEL. Showing a clear boundary of  $L_{2-10} \approx 2.6 \times 10^{42} \text{ erg s}^{-1}$  for the disappearance of the broad  $H\alpha$  component.

a decline in the  $H\alpha$  BEL flux. In 2021 March we measured a flux of  $\sim 25 \times 10^{-13} \text{ erg cm}^{-2} \text{ s}^{-1}$ , while in 2021 April the flux was  $\sim 18 \times 10^{-13} \text{ erg cm}^{-2} \text{ s}^{-1}$ . The same trend is present in the  $H\beta$  flux, which evolves from undetected in 2006 to an increase from 2014 until 2018, and finally declining in 2021. Within the uncertainties the Balmer decrements seems to be constant at a value of  $\sim 9$ .

### 3.3 The Link Between the X-ray Luminosity and the BELs

Comparing the middle and bottom panels of Fig. 1, one can promptly see a correlation between the intrinsic X-ray luminosity and the detection of the broad  $H\alpha$  component. The periods in which the broad component is detectable are the ones where  $L_{2-10}$  shows the highest values; epochs in which the galaxy is classified as a Seyfert 2 are those when the closest available X-ray spectra show lower  $L_{2-10}$  values. Given that the X-ray and optical observations are not simultaneous, in order to quantify the correlation between the BELs and the X-ray luminosity we linearly interpolate the  $L_{2-10}$  curve (bottom panel of Fig. 1) and attribute an  $L_{2-10}$  value for each historical optical spectrum. In Fig. 5 we show the interpolated  $L_{2-10}$  value for each spectrum as function of the corresponding  $H\alpha$  BEL detection.

From Fig. 5, the link between the BEL and the X-ray luminosity is clear: at all epochs when an  $H\alpha$  BEL is not detected,  $L_{2-10} < 2.6 \times 10^{42} \text{ erg s}^{-1}$  (the X-ray luminosity of the bright Seyfert 2 spectra); conversely, when a Seyfert 1.x spectrum is observed,  $L_{2-10} > 2.6 \times 10^{42} \text{ erg s}^{-1}$ . Moreover, from Fig. 4 (top panels) we can see that for the modern spectra (2006–2021) the  $H\alpha$  BEL flux increases with the increase in the  $L_{2-10}$ . From the same figures, we can see that the transitions from Type 1.9 to Type 1.8 (i.e. the clear detection of the  $H\beta$  BEL) also seems to be synchronous to  $L_{2-10}$ . It is possible that the oldest high Eddington Ratio optical observations did not detect the broad  $H\beta$  due to its faintness or lower signal-to-noise ratio.

We can convert the transitional X-ray luminosity ( $2.6 \times 10^{42} \text{ erg s}^{-1}$ ) into a Bolometric luminosity ( $L_{\text{bol}}$ ) and then into the Eddington ratio ( $\lambda_{\text{Edd}}$ ), as follows:

$$\lambda_{\text{Edd}} = \frac{L_{\text{Bol}}}{L_{\text{Edd}}} = \frac{[K_X(L_{2-10}) \pm \Delta K_X] \times L_{2-10}}{1.3 \times 10^{38} M_{\text{BH}}}, \quad (3)$$

where  $K_X$  is the bolometric correction and  $\Delta K_X$  is uncertainty in the bolometric correction (the intrinsic spread of the AGN population

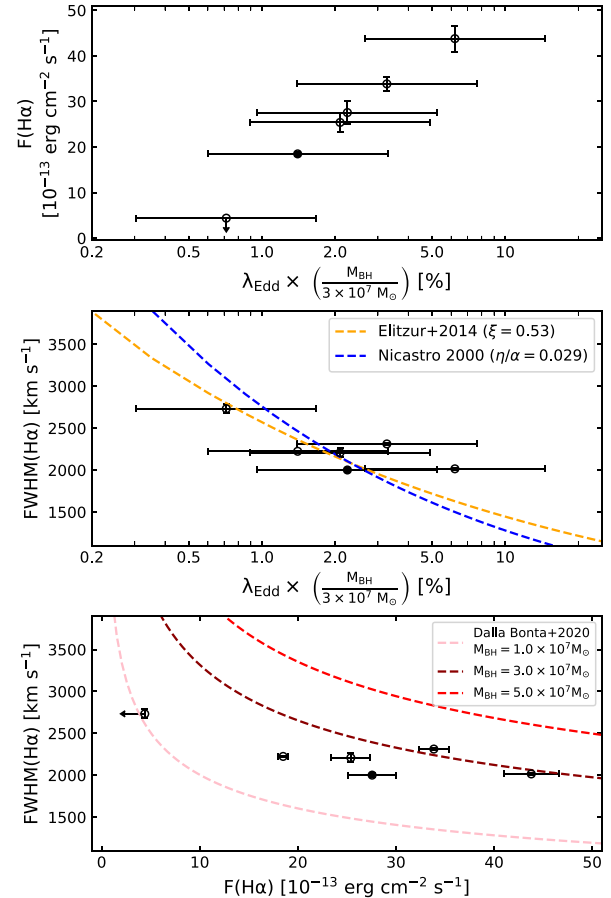


**Figure 6.** Top: flux of  $H\alpha$  BEL as function of Eddington Ratio ( $\lambda_{\text{Edd}}$ ), measured using equations (3) and (4), for each modern optical spectrum. Middle: FWHM of  $H\alpha$  BEL as function of  $\lambda_{\text{Edd}}$  for each modern optical spectrum. Blue and orange dashed lines are, respectively, presents the best-fitting Nicastro (2000) and Elitzur et al. (2014) BLR models (see Section 3.3 and equations 5 and 6). The term  $(3 \times 10^7 M_{\odot} / M_{\text{BH}})$  is written as a systematic scaling factor to take into account the uncertainties in the black hole mass and the distinct values that can be considered (see Section 2.5). Bottom: FWHM of  $H\alpha$  BEL as function of  $H\alpha$  BEL flux for each modern optical spectrum. The dashed lines represent the Dalla Bontà et al. (2020) relation between the two parameters, assuming a constant Balmer decrement of nine and Calzetti et al. (2000) extinction law, for distinct SMBHs ( $M_{\text{BH}}$ ) in the range discussed in Section 2.5.

dominates this uncertainty). We use Duras et al. (2020) correction, which assumes values of  $K_X(L_{2-10} = 2.6 \times 10^{42} \text{ erg s}^{-1}) = 15.54$  and  $\Delta K_X = 0.37$  dex. Therefore, the Eddington ratio at which the  $H\alpha$  BEL disappears can be written as:

$$\lambda_{\text{Edd}} \approx 1.1^{+1.4}_{-0.7} \times \left( \frac{3 \times 10^7 M_{\odot}}{M_{\text{BH}}} \right) \%, \quad (4)$$

where the term  $(3 \times 10^7 M_{\odot} / M_{\text{BH}})$  is written as a systematic scaling factor to take into account the uncertainties in the black hole mass and the distinct values that can be considered (see Section 2.5). Using the same prescription, we show in the top panel of Fig. 6 the clear correlation between the measured  $H\alpha$  BEL fluxes and  $\lambda_{\text{Edd}}$ . Assuming the above predicted transitional X-ray luminosity ( $2.6 \times 10^{42} \text{ erg s}^{-1}$ ) is correct, the AGN should be at its Seyfert 2 state as of 2021 June (see Table 1). Unfortunately, we were not able to get a new optical spectrum, given that the galaxy is not visible in the sky at the time of this publication. We will try to do a follow-up

observation as soon as the galaxy becomes visible again, in 2021 November, in order to confirm this hypothesis.

In summary, this analysis strongly supports the hypothesis that the CL phenomenon in NGC 2992 is caused by variations in the accretion rate and not due to changes in absorption nor due to TDEs (which we discard due to the several repeated CL events).

In the last several years, the idea that the orientation-based unification models alone cannot explain the variety of AGNs (see Spinoglio & Fernández-Ontiveros 2019, for a review of challenges to the unification model), and that the specific accretion rate, as given by the Eddington ratio, is as essential as obscuration in the classification of the distinct AGN types, has been explored by several authors. For example, Trump et al. (2011) using a sample of 118 unobscured ( $N_{\text{H}} < 10^{22} \text{ cm}^{-2}$ ) AGNs show that the BELs are present only at the highest accretion rates ( $\lambda_{\text{Edd}} > 1$  per cent).

Several authors have proposed models that posit different accretion rates as a cause of the differences between observed AGNs (see Ho 2008, for a review of the properties of low luminosity AGNs). Elitzur & Ho (2009) suggest that the BLR and ‘torus’ are inner (ionized) and outer (clumpy and dusty) parts of the same disc-driven wind and that this wind is no longer supported at low accretion rates (Nicastrò 2000; Elitzur & Shlosman 2006; Nenkova et al. 2008). Based on this disc-wind BLR model, Elitzur et al. (2014) proposed that the intrinsic spectral sequence  $S1 \rightarrow S1.2/S1.5 \rightarrow S1.8/S1.9 \rightarrow S2^2$  is a true evolutionary sequence, reflecting the evolution of the BLR structure with decreasing accretion rate on to the central black hole and that this evolution is regulated by the  $L_{\text{bol}}/M_{\text{BH}}^{2/3}$  variable (which behaves like  $\lambda_{\text{Edd}}$ ). These models have been successfully used to explain the existence of ‘true’ Type 2 Seyferts as shown by Marinucci et al. (2012) and are recently being invoked to explain CL-AGNs.

### 3.4 Proposed scenarios

We have shown that the variability in NGC 2992 is intrinsically driven by changes in accretion rate, and not due to variable obscuration. In this scenario, the CL events (i.e. the disappearing and reappearing of the BELs) can be due to two distinct effects:

(i) Dimming or brightening of the AGN continuum, which changes the supply of ionizing photons available to excite the gas in the immediate vicinity of the black hole and therefore the BLR. In this case, variations in the BEL fluxes are due to changes in the ionization state of the BLR clouds and not to change in its geometry or structure (Storchi-Bergmann et al. 2003; Schimoia et al. 2012; LaMassa et al. 2015);

(ii) The fading of the BLR structure itself as proposed by the disc-wind BLR models (Elitzur & Shlosman 2006; Elitzur & Ho 2009), in which a low accretion rate is not able to sustain the required cloud flow rate (Nicastrò 2000; Trump et al. 2011; Elitzur et al. 2014), which makes up the BLR.

The first scenario is supported in the case of the double-peaked LINER/Seyfert 1 nucleus of NGC 1097, for which Storchi-Bergmann et al. (2003) and Schimoia et al. (2012) found an inverse correlation between the width of the  $H\alpha$  broad profile and the flux of the line, as well as for NGC 5548 by Peterson et al. (2002) and for the CL-Quasar SDSS J015957.64+003310.5 by LaMassa et al. (2015). The

<sup>2</sup>Referring here only to the ‘true’ Type 2 Seyferts, meaning those which do not have BELs even in polarized light, therefore excluding those which have obscured Type 1 nucleus.

authors preferred explanation for this is the fact that, when the AGN is brightest, it ionizes farther out in the BLR, reaching lower velocity clouds, and the profile becomes narrower. When the AGN is dimmer, it ionizes only the closest regions, where the velocities are higher and the profile becomes wider, in agreement with a virialized BLR. In our data, there seems to be such an inverse correlation between  $\text{FWHM}(H\alpha)$  and  $F(H\alpha)$  in the modern optical spectra, as can be seen in the bottom panel of Fig. 6.

However, in the second scenario, where the BLR is described as a disc-driven wind and not as clouds orbiting in Keplerian-like orbits, this inverse correlation is also predicted. Using distinct prescriptions both Nicastrò (2000) and Elitzur et al. (2014) show that with increasing accretion rate ( $\lambda_{\text{Edd}}$ ) (which increases  $H\alpha$  BEL flux) the FWHM in the BLR decreases. In the Nicastrò (2000) model, the relation between the two parameters is written as:

$$\log(\lambda_{\text{Edd}}) = -3\log(\text{FWHM}) + 9.86 + \log(\eta/\alpha), \quad (5)$$

where  $\eta/\alpha$  is the ratio between the disc efficiency ( $\eta$ ) and its viscosity ( $\alpha$ ), while Elitzur et al. (2014) use:

$$\log(\lambda_{\text{Edd}}) = -4\log(\text{FWHM}) + 3.60 + \log(M_{\text{BH}}) + \log(\xi), \quad (6)$$

where  $\xi$  is the ratio between the BLR radius ( $r_{\text{BLR}}$ ) and the dust sublimation radius ( $R_d$ ) with  $\xi < 1.0$ . The reader is referred to the original papers as well as to Nicastrò, Mathur & Krongold (2018) for detailed explanation of the models and equations. In the middle panel of Fig. 6, we show both models with best-fitting parameters ( $\eta/\alpha = 0.029$  and  $\xi = 0.53$ ) for the measured  $H\alpha$  BEL FWHM and  $\lambda_{\text{Edd}}$ , measured from the interpolated  $L_{2-10}$  (Fig. 5) using the above prescription (equations 3 and 4).

While we have successfully shown that the CL events in NGC 2992 are driven by changes in the accretion rate, we could not determine the true nature of the BEL variability, mainly because, as discussed, we still do not have a full understanding of the formation and evolution of the BLRs in AGNs. In the next section we discuss the overall state-of-art modelling of the innermost structure of active galaxies as well as a proposed technique to distinguish between the two above proposed scenarios.

## 4 RESULTS AND DISCUSSION

In both the scenarios discussed in the previous section, quick ( $\sim 10$  yr between the maximum and the minimum activity) and large (a factor of  $\sim 40$  in  $L_{2-10}$ ) variations in the accretion rate are necessary. However, the standard Shakura & Sunyaev (1973) accretion disc model does not support such variations given that for AGN scales (where the model still predicts the existence of a geometrically thin disc,  $H \ll R$ ) the viscous time-scale of the disc is in the order of  $10^4$  to  $10^5$  yr, greatly exceeding the time-scales over which CL transitions are known to occur. This incompatibility was noticed long ago (e.g. Koratkar & Blaes 1999; Antonucci 2013), but just recently some modification or alternatives to the application of Shakura & Sunyaev (1973) model to AGNs have been proposed in light of the increasing number of these CL sources been discovered.

For example, Dexter & Begelman (2018) propose that AGN accretion discs are vertically supported by magnetic pressure, which makes it geometrically thick ( $H/R$  between 0.1 and 1.0) at all luminosities. Jiang & Blaes (2020) show, for a  $5 \times 10^8 M_{\odot}$  mass black hole, using three dimensional radiation magneto-hydrodynamic simulations, which under this assumption the Rosseland mean opacity is expected to be larger than the electron scattering value, and the iron opacity bump then causes the disc to be convectively unstable. This results in strong fluctuations in surface density and heating of the

disc. The opacity drops with increasing temperature and convection is suppressed. The disc cools down and the whole process repeats. This causes strong oscillations of the disc scale height and luminosity variations by more than a factor of  $\approx 3\text{--}6$  over time-scales of few years. They argue that since the iron opacity bump will move to different locations of the disc for black holes with different masses and accretion rates, this is a physical mechanism that can explain the accretion rate variability of AGN with a wide range of amplitudes over a time-scale of years to decades.

The Eddington ratio in which the BEL transitions occurs in NGC 2992 contains the critical value at which there is a state transition between a radiatively inefficient accretion flow (RIAF) and a thin accretion disc ( $\lambda_{\text{Edd}} \sim 1$  per cent; e.g. Ho 2008; Xie & Yuan 2012). The similarity between these values suggests that NGC 2992 is operating at the threshold mass accretion rate between the two accretion modes. Indeed, Sniegowska et al. (2020) proposed an explanation for the sources displaying multiple quasi-periodic CL phenomena according to which they would be operating at a few per cent of the Eddington limit. They argue that the outbursts are caused by the radiation pressure instability operating in the narrow ring between the standard (Shakura & Sunyaev 1973) thin pressure dominated outer disc and the hot optically thin inner RIAF (Yuan & Narayan 2014). The corresponding limit cycle is responsible for periodic outbursts, and the time-scales are therefore much shorter than the standard viscous time-scale due to the narrowness of the unstable radial zone.

Even with the possibility of such rapid variability in the accretion rate (given some of these alternatives to the classical accretion disc) the cause of the type transition remains uncertain, dimming of the ionizing source or fading of the BLR structure itself. By using radiative transfer Monte Carlo simulations to test the multiple causes of the CL phenomenon, Marin (2017) argues that the differences between these two scenarios can only be observable in polarized light: in the ionizing source dimming scenario the polarization properties between the high and low flux state should be the same, while that for the BLR fading a decrease in the degree of polarization and a rotation in the polarization angle are expected in the low flux state. We had access to a spectropolarimetric observation of NGC 2992 obtained in 2006 (Robinson et al., in preparation), when the galaxy was at a dim state (see Fig. 1). It shows no signs of BEL in the polarimetric spectrum (as well as in normal flux). In order to test Marin (2017) predictions, we would need another polarimetric spectrum, with the AGN at its bright state. As this data is not available for now, the exact intrinsic cause of the CL-AGN events in NGC 2992 is still an open question. We join these authors in advocating for systematic polarimetric observations of CL-AGN in order to fully understand their true nature. In this sense, follow-up observations (polarimetric or not) of NGC 2992 in the next decades will continue to help constrain the physics of AGNs. Furthermore, this source joins several others in the literature that show that the accretion rate is a fundamental variable for any model that tries to unify the AGN zoology, and that viewing angle or obscuration effects alone cannot fully explain differences seen in SMBH activity in galaxies.

## 5 CONCLUSIONS

We have analysed historical X-ray and optical observations of the Seyfert galaxy NGC 2992, from 1978 to 2021 – as well as presented new X-ray and optical spectra – focusing on its CL events. The main conclusions are:

- (i) The source presents large intrinsic X-ray luminosity variability ranging from  $4.9 \times 10^{41}$  erg s $^{-1}$  up to  $2.0 \times 10^{43}$  erg s $^{-1}$ ;
- (ii) Several transitions between Type 2 Seyfert and intermediate-types are documented, with the appearance and disappearance of the H $\alpha$  BEL occurring on time-scales of several years;
- (iii) We ruled out TDEs or variable obscuration as causes of the type transitions. We show that the flux of the H $\alpha$  BEL is directly correlated with the 2–10 keV X-ray luminosity: the H $\alpha$  BEL seems to disappear at  $L_{2-10}$  values lower than  $2.6 \times 10^{42}$  erg s $^{-1}$ . This value translates to an Eddington ratio of  $1.1_{-0.7}^{+1.4}$  per cent, if we assume  $M_{\text{BH}} = 3 \times 10^7 M_{\odot}$ .
- (iv) We find a correlation between the narrow Fe K $\alpha$  line flux and  $\lambda_{\text{Edd}}$ , and an anticorrelation between full width at half maximum of the H $\alpha$  BEL and  $\lambda_{\text{Edd}}$ , as predicted by theoretical work by Nicastro (2000) and Elitzur (2012).
- (v) Two possible scenarios for type transitions are still open: either the dimming (brightening) of the AGN continuum luminosity, which reduces (increases) the supply of ionizing photons available to excite the gas in the immediate vicinity of the black hole (LaMassa et al. 2015) or the disappearance of the BLR structure itself occurs as the low accretion efficiency is not able to sustain the required cloud flow rate in a disc-wind BLR model (Elitzur & Shlosman 2006; Trump et al. 2011; Elitzur et al. 2014). Multi-epoch polarimetric observations may distinguish between the two scenarios.
- (vi) This study supports the idea that the accretion rate is a fundamental variable in determining the observed AGN type, and therefore should be included in a more complete model to unify the AGN zoology.

## ACKNOWLEDGEMENTS

We would like to thank all those authors and observatories that made public their data making this work possible, specially Michael Crenshaw for providing the Trippe et al. (2008) spectrum and Adam Thomas for helping us access the S7 survey (Dopita et al. 2015) data. We also thank Gemini’s and SOAR’s staff, in special Luciano Fraga, for their rapid response on accepting and observing our DDT proposals. MGP also would like to thanks Michael Fausnaugh for making MAPSPEC publicly available as well as for his comments and suggestions on the paper.

Based in part on observations obtained at the Southern Astrophysical Research (SOAR) telescope, which is a joint project of the Ministério da Ciência, Tecnologia e Inovações (MCTI/LNA) do Brasil, the US National Science Foundation’s NOIRLab, the University of North Carolina at Chapel Hill (UNC), and Michigan State University (MSU). Based on observations obtained at the international Gemini Observatory, a program of NSF’s NOIRLab, which is managed by the Association of Universities for Research in Astronomy (AURA) under a cooperative agreement with the National Science Foundation on behalf of the Gemini Observatory partnership: the National Science Foundation (United States), National Research Council (Canada), Agencia Nacional de Investigación y Desarrollo (Chile), Ministerio de Ciencia, Tecnología e Innovación (Argentina), Ministério da Ciência, Tecnologia, Inovações e Comunicações (Brazil), and Korea Astronomy and Space Science Institute (Republic of Korea). We acknowledge the use of public data from the *Swift* data archive.

## DATA AVAILABILITY

The GMOS, MUSE, and *Swift* data are publicly available at the Gemini, ESO, and HEASARC archive web pages, respectively. The

other data underlying this article will be shared on reasonable request to the corresponding author.

## REFERENCES

- Allen M. G., Dopita M. A., Tsvetanov Z. I., Sutherland R. S., 1999, *ApJ*, 511, 686
- Andrillat Y., Souffrin S., 1971, *A&A*, 11, 286
- Antonucci R., 1993, *ARA&A*, 31, 473
- Antonucci R., 2013, *Nature*, 495, 165
- Arexaga I., Joguet B., Kunth D., Melnick J., Terlevich R. J., 1999, *ApJ*, 519, L123
- Arnaud K. A., 1996, in Jacoby G. H., Barnes J., eds, ASP Conf. Ser. Vol. 101, *Astronomical Data Analysis Software and Systems V*. Astron. Soc. Pac., San Francisco, p. 17
- Avni Y., 1976, *ApJ*, 210, 642
- Barlow R., 2003, in Lyons L., Mount R., Reitmeyer R., eds, *Statistical Problems in Particle Physics, Astrophysics, and Cosmology*. Stanford, USA, p. 250
- Barlow R., 2004, *Asymmetric Statistical Errors*. preprint ([arXiv:physics/0406120](https://arxiv.org/abs/physics/0406120))
- Bianchi S., Piconcelli E., Chiaberge M., Bailón E. J., Matt G., Fiore F., 2009, *ApJ*, 695, 781
- Burrows D. N. et al., 2005, *Space Sci. Rev.*, 120, 165
- Busko I. C., Steiner J. E., 1990, *MNRAS*, 245, 470
- Calzetti D., Armus L., Bohlin R. C., Kinney A. L., Koornneef J., Storchi-Bergmann T., 2000, *ApJ*, 533, 682
- Cid Fernandes R., Mateus A., Sodré L., Stasińska G., Gomes J. M., 2005, *MNRAS*, 358, 363
- Cohen R. D., Rudy R. J., Puetter R. C., Ake T. B., Foltz C. B., 1986, *ApJ*, 311, 135
- Cooke B. A. et al., 1978, *MNRAS*, 182, 489
- Corral A., Della Ceca R., Caccianiga A., Severgnini P., Brunner H., Carrera F. J., Page M. J., Schwobe A. D., 2011, *A&A*, 530, A42
- Dai X., Chartas G., Eracleous M., Garmire G. P., 2004, *ApJ*, 605, 45
- Dalla Bontà E. et al., 2020, *ApJ*, 903, 112
- Denney K. D. et al., 2014, *ApJ*, 796, 134
- Dexter J., Begelman M. C., 2018, *MNRAS*, 483, L17
- Dopita M. A. et al., 2015, *ApJS*, 217, 12
- Duras F. et al., 2020, *A&A*, 636, A73
- Durret F., Bergeron J., 1988, *A&AS*, 75, 273
- Elitzur M., 2012, *ApJ*, 747, L33
- Elitzur M., Ho L. C., 2009, *ApJ*, 701, L91
- Elitzur M., Shlosman I., 2006, *ApJ*, 648, L101
- Elitzur M., Ho L. C., Trump J. R., 2014, *MNRAS*, 438, 3340
- Eracleous M., Halpern J. P., 2001, *ApJ*, 554, 240
- Eracleous M., Livio M., Halpern J. P., Storchi-Bergmann T., 1995, *ApJ*, 438, 610
- Fausnaugh M. M., 2017, *PASP*, 129, 024007
- García-Lorenzo B., Arribas S., Mediavilla E., 2001, *A&A*, 378, 787
- Gilli R., Maiolino R., Marconi A., Risaliti G., Dadina M., Weaver K. A., Colbert E. J. M., 2000, *A&A*, 355, 485
- Graham M. J. et al., 2020, *MNRAS*, 491, 4925
- Gültekin K. et al., 2009, *ApJ*, 698, 198
- Guo H., Sun M., Liu X., Wang T., Kong M., Wang S., Sheng Z., He Z., 2019, *ApJ*, 883, L44
- Guolo-Pereira M., Ruschel-Dutra D., Storchi-Bergmann T., Schnorr-Müller A., Cid Fernandes R., Gouto G., Dametto N., Hernandez-Jimenez J. A., 2021, *MNRAS*, 502, 3618
- Hill J. E. et al., 2004, in Flanagan K. A., Siegmund O. H. W., eds, Proc. SPIE Conf. Ser. Vol. 5165, *X-Ray and Gamma-Ray Instrumentation for Astronomy XIII*. SPIE, Bellingham, p. 217
- Ho L. C., 2008, *ARA&A*, 46, 475
- Jiang Y.-F., Blaes O., 2020, *ApJ*, 900, 25
- Kalberla P. M. W., Burton W. B., Hartmann D., Arnal E. M., Bajaja E., Morras R., Pöppel W. G. L., 2005, *A&A*, 440, 775
- Keel W. C., 1996, *ApJS*, 106, 27
- Kollatschny W., Ochmann M. W., Zetzl M., Haas M., Chelouche D., Kaspi S., Pozo Nuñez F., Grupe D., 2018, *A&A*, 619, A168
- Kollatschny W. et al., 2020, *A&A*, 638, A91
- Koratkar A., Blaes O., 1999, *PASP*, 111, 1
- LaMassa S. M. et al., 2015, *ApJ*, 800, 144
- Lampton M., Margon B., Bowyer S., 1976, *ApJ*, 208, 177
- Lawrence A., 2018, *Nature Astron.*, 2, 102
- Lepine J. R. D. et al., 2003, in Iye M., Moorwood A. F. M., eds, Proc. SPIE Conf. Ser. Vol. 4841, *Instrument Design and Performance for Optical/Infrared Ground-based Telescopes*. SPIE, Bellingham, p. 1086
- Liu H., Wu Q., Lyu B., Yan Z., 2019, Evidence for Changing-Look Agns is Caused by Change of Accretion Mode. preprint ([arXiv:1912.03972](https://arxiv.org/abs/1912.03972))
- Maccacaro T., Perola G. C., Elvis M., 1982, *ApJ*, 257, 47
- MacLeod C. L. et al., 2016, *MNRAS*, 457, 389
- Marchese E., Braitto V., Della Ceca R., Caccianiga A., Severgnini P., 2012, *MNRAS*, 421, 1803
- Marin F., 2017, *A&A*, 607, A40
- Marinucci A., Bianchi S., Nicastro F., Matt G., Goulding A. D., 2012, *ApJ*, 748, 130
- Marinucci A., Risaliti G., Wang J., Bianchi S., Elvis M., Matt G., Nardini E., Braitto V., 2013, *MNRAS*, 429, 2581
- Marinucci A., Bianchi S., Braitto V., Matt G., Nardini E., Reeves J., 2018, *MNRAS*, 478, 5638
- Marinucci A., Bianchi S., Braitto V., De Marco B., Matt G., Middei R., Nardini E., Reeves J. N., 2020, *MNRAS*, 496, 3142
- Marquez I., Boisson C., Durret F., Petitjean P., 1998, *A&A*, 333, 459
- Matt G., Guainazzi M., Maiolino R., 2003, *MNRAS*, 342, 422
- McElroy R. E. et al., 2016, *A&A*, 593, L8
- Mingozzi M. et al., 2019, *A&A*, 622, A146
- Murphy K. D., Yaqoob T., Terashima Y., 2007, *ApJ*, 666, 96
- Murphy K. D., Nowak M. A., Marshall H. L., 2017, *ApJ*, 840, 120
- Mushotzky R. F., 1982, *ApJ*, 256, 92
- Nandra K., Pounds K. A., 1994, *MNRAS*, 268, 405
- Nelson C. H., Whittle M., 1995, *ApJS*, 99, 67
- Neškova M., Sirocky M. M., Nikutta R., Ivezić Ž., Elitzur M., 2008, *ApJ*, 685, 160
- Nicastro F., 2000, *ApJ*, 530, L65
- Nicastro F., Mathur S., Krongold Y., 2018, When a seyfert...has a crash on a model
- Oknyansky V. L., Winkler H., Tsygankov S. S., Lipunov V. M., Gorbovskoy E. S., van Wyk F., Buckley D. A. H., Tyurina N. V., 2019, *MNRAS*, 483, 558
- Osmer P. S., Smith M. G., Weedman D. W., 1974, *ApJ*, 192, 279
- Osterbrock D. E., 1981, *ApJ*, 249, 462
- Osterbrock D. E., Ferland G. J., 2006, *Astrophysics of gaseous nebulae and active galactic nuclei*, 2nd edn., Univ. Science Books, Sausalito, CA
- Pastoriza M., Gerola H., 1970, *Astrophys. Lett.*, 6, 155
- Peterson B. M., 1993, *PASP*, 105, 247
- Peterson B. M., Pogge R. W., Wanders I., Smith S. M., Romanishin W., 1995, *PASP*, 107, 579
- Peterson B. M. et al., 2002, *ApJ*, 581, 197
- Ponti G., Papadakis I., Bianchi S., Guainazzi M., Matt G., Uttley P., Bonilla N. F., 2012, *A&A*, 542, A83
- Possolo A., Merkatas C., Bodnar O., 2019, *Metrologia*, 56, 045009
- Ptak A., Yaqoob T., Murphy K., SUZAKU Ngc 2992 Team, 2007, *Prog. Theor. Phys. Suppl.*, 169, 252
- Puccetti S., Fiore F., Risaliti G., Capalbi M., Elvis M., Nicastro F., 2007, *MNRAS*, 377, 607
- Qiao E., Liu B. F., 2013, *ApJ*, 764, 2
- Ricci C., Ueda Y., Paltani S., Ichikawa K., Gandhi P., Awaki H., 2014, *MNRAS*, 441, 3622
- Risaliti G., Elvis M., Bianchi S., Matt G., 2010, *MNRAS*, 406, L20
- Ruan J. J. et al., 2016, *ApJ*, 826, 188
- Runnoe J. C. et al., 2016, *MNRAS*, 455, 1691
- Ruschel-Dutra D., de Oliveira B. D., 2020, *danielrd6/ifscube: Modeling Schimoia J. S., Storchi-Bergmann T., Nemmen R. S., Winge C., Eracleous M., 2012, ApJ, 748, 145*
- Schnorr-Müller A. et al., 2016, *MNRAS*, 462, 3570

- Shakura N. I., Sunyaev R. A., 1973, *A&A*, 500, 33
- Shappee B. J. et al., 2014, *ApJ*, 788, 48
- Sheng Z., Wang T., Jiang N., Yang C., Yan L., Dou L., Peng B., 2017, *ApJ*, 846, L7
- Shu X. W., Yaqoob T., Murphy K. D., Braito V., Wang J. X., Zheng W., 2010, *ApJ*, 713, 1256
- Shuder J. M., 1980, *ApJ*, 240, 32
- Sniegowska M., Czerny B., Bon E., Bon N., 2020, *A&A*, 641, A167
- Spinoglio L., Fernández-Ontiveros J. A., 2019, in Mirjana P., ed., *Proc. IAU Symp. 15, Nuclear Activity in Galaxies Across Cosmic Time*. Cambridge Univ. Press, Cambridge, p. 29
- Stoklasová I., Ferruit P., Emsellem E., Jungwiert B., Pécontal E., Sánchez S. F., 2009, *A&A*, 500, 1287
- Storchi-Bergmann T., Schnorr-Müller A., 2019, *Nature Astron.*, 3, 48
- Storchi-Bergmann T., Baldwin J. A., Wilson A. S., 1993, *ApJ*, 410, L11
- Storchi-Bergmann T. et al., 2003, *ApJ*, 598, 956
- Swank J. H., 2006, *Adv. Space Res.*, 38, 2959
- Theureau G., Hanski M. O., Coudreau N., Hallet N., Martin J.-M., 2007, *A&A*, 465, 71
- Tohline J. E., Osterbrock D. E., 1976, *ApJ*, 210, L117
- Tremaine S. et al., 2002, *ApJ*, 574, 740
- Trippe M. L., Crenshaw D. M., Deo R., Dietrich M., 2008, *AJ*, 135, 2048
- Trump J. R. et al., 2011, *ApJ*, 733, 60
- Turner T. J., Pounds K. A., 1989, *MNRAS*, 240, 833
- Urry C. M., Padovani P., 1995, *PASP*, 107, 803
- van Groningen E., Wanders I., 1992, *PASP*, 104, 700
- Veilleux S., Shopbell P. L., Miller S. T., 2001, *AJ*, 121, 198
- Veron P., Lindblad P. O., Zuiderwijk E. J., Veron M. P., Adam G., 1980, *A&A*, 87, 245
- Wang J., Xu D. W., Wang Y., Zhang J. B., Zheng J., Wei J. Y., 2019, *ApJ*, 887, 15
- Ward M., Penston M. V., Blades J. C., Turtle A. J., 1980, *MNRAS*, 193, 563
- Weaver K. A., Nousek J., Yaqoob T., Mushotzky R. F., Makino F., Otani C., 1996, *ApJ*, 458, 160
- Winter L. M., Mushotzky R. F., Reynolds C. S., Tueller J., 2009, *ApJ*, 690, 1322
- Woo J.-H., Urry C. M., 2002, *ApJ*, 579, 530
- Xie F.-G., Yuan F., 2012, *MNRAS*, 427, 1580
- Yang Q. et al., 2018, *ApJ*, 862, 109
- Yaqoob T., 1998, *ApJ*, 500, 893
- Yaqoob T. et al., 2007, *PASJ*, 59, S283
- Yuan F., Narayan R., 2014, *ARA&A*, 52, 529

## APPENDIX A: PROPAGATION OF ASYMMETRIC UNCERTAINTIES

When the underlying likelihood function of a parameter is not symmetric, the error distribution will also be asymmetric. Different origins of asymmetry are discussed in detail by Barlow (2003, 2004). In high-energy astrophysics it is related to the low photon counting. In this case, the estimated parameters are usually reported in a form like  $\hat{x}_{-u_l}^{+u_r}$ , where  $\hat{x}$  is the best-fitting parameter (minimum  $\chi^2$ ) and  $u_l$  and  $u_r$  are the draw where the  $\Delta\chi^2$  curve reaches some value, for

classical  $1\sigma$  (68 per cent) confidence level  $\Delta\chi^2 = 1.0$ ; however the 90 per cent confidence level ( $\Delta\chi^2 = 2.7$ ) is the most employed in X-ray astronomy (Avni 1976; Lampton, Margon & Bowyer 1976; Yaqoob 1998).

Usually, one needs to calculate a function of one or more quantities, and propagate its uncertainties. In most circumstances, well-known ‘Error Propagation’ formulas are adequate. But there are some assumptions and approximations under the error propagation, and if they fail, the method is invalid. These assumptions can be summarized as: the errors are normally distributed (Gaussian errors) and they are relatively small. For asymmetric errors in astronomy any of these assumptions can be made; if the asymmetry is really small, rounding or averaging the negative and the positive errors into a single value and making the distribution symmetric does not change the result much. But when the values are not appropriate to do that, researchers often tend to put two error values into quadrature separately and combine them in the result. Actually this is not a valid method due to violation of the Central Limit Theorem (Barlow 2003). Eventually more sophisticated methods are needed to use: we present here a Python-based Monte Carlo solution for this problem, based in a combination of Barlow (2004) and Possolo et al. (2019) derivations.

During this research we faced the problem that even with numerous of uncertainties propagation tools publicly available (e.g. `astropy.uncertainty`, `uncertainties`), none of them are able to handle asymmetric uncertainties as we needed due to the assumptions stated above. We therefore created the `ASYMMETRICUNCERTAINTIES` Python package: the main idea of the code is to generate a random sample from the likelihood function and use this sample in other calculations (Possolo et al. 2019). The code assumes a ‘Variable Width Gaussian’ likelihood, which, as shown by Barlow (2004), reproduces very well the underlying likelihood of low counting measurements, and, in contrast to, for example, a ‘Generalized Poisson’ distribution, has a unique and analytical solution for given values of  $\hat{x}$ ,  $u_l$ , and  $u_r$  at a given confidence level ( $\Delta\chi^2$ ). From this likelihood the code generates a random sample of data that can be passed as parameters for any type of function. Simple operations are dealt internally by the code and the more sophisticated ones can be easily performed by the user, for example:  $L_{2-10}$  values in Table 1 whose uncertainties were propagated from  $\Gamma$  and  $N_H$  uncertainties, as well as the statistical tests ( $r_s$  and  $p_{\text{value}}$ ) in Fig. 2. The resulting sample is then fitted by the code returning the nominal value and the propagated uncertainties. The code is publicly available at github,<sup>3</sup> where examples in how to use the code are also presented.

<sup>3</sup>[https://github.com/muryelgp/asymmetric\\_uncertainties](https://github.com/muryelgp/asymmetric_uncertainties)

This paper has been typeset from a  $\text{\TeX}/\text{\LaTeX}$  file prepared by the author.